AN ASSESSMENT OF 3-C PIV ANALYSIS METHODOLOGY FOR HART II MEASURED DATA

Joon W. Lim
Aeroflightdynamics Directorate
Aviation Missile Research, Development,
and Engineering Command
Ames Research Center
Moffett Field, California

and

Berend G. van der Wall
German Aerospace Center (DLR)
Institute of Flight Systems
Braunschweig, Germany

July 2010

DESTRUCTION NOTICE

DISCLAIMER

TRADE NAMES

REPORT DOCUMENTATION PAGE

Form Approved
OMB No. 074-0188

Public reporting burden for this collection of information is estimated to average 1 hour per response, including the time for reviewing instructions, searching existing data sources, gathering and maintaining the data needed, and completing and reviewing this collection of information. Send comments regarding this burden estimate or any other aspect of this collection of information, including suggestions for reducing this burden to Washington Headquarters Services, Directorate for Information Operations and Reports, 1215 Jefferson Davis Highway, Suite 1204, Arlington, VA 22202-4302, and to the Office of Management and Budget, Paperwork Reduction Project (0704-0188), Washington, DC 20503

1. AGENCY USE ONLY	2. REPORT DATE July 2010	3. REPORT TYPE AND DATES COVERED Technical Report

4. TITLE AND SUBTITLE

An Assessment of 3-C PIV Analysis Methodology for HART II Measured Data

5. FUNDING NUMBERS

6. AUTHOR(S)

Joon W. Lim and Berend G. van der Wall

7. PERFORMING ORGANIZATION NAME(S) AND ADDRESS(ES)
Commander, U.S. Army Research, Development, and
   Engineering Command
ATTN: RDMR-AF
Redstone Arsenal, AL 35898

8. PERFORMING ORGANIZATION REPORT NUMBER

TR-RDMR-AF-10-03
NASA/TM-2010-216024

9. SPONSORING / MONITORING AGENCY NAME(S) AND ADDRESS(ES)

10. SPONSORING / MONITORING AGENCY REPORT NUMBER

11. SUPPLEMENTARY NOTES
   POC: Joon W. Lim, NASA-Ames Research Center, M/S 215-1, Bldg 215, Moffett Field, CA 94035
lim@merlin.arc.nasa.gov

12a. DISTRIBUTION / AVAILABILITY STATEMENT

Approved for public release; distribution is unlimited.

12b. DISTRIBUTION CODE

A

13. ABSTRACT *(Maximum 200 Words)*

   Since the completion of the DNW test, HART II partners have put forth significant efforts to derive vortex properties from the measured data. These properties include vortex center, rotation angles of the vortex axis in the PIV measurement plane, maximum vorticity, core radius , and swirl velocity. Differences among the partners' results were found for some of these vortex properties, which required more effort to assess the physical significance of the differences. This was because the derived vortex properties were an integral of all the sub-processes in the complex PIV data analysis procedure, and more information was needed to resolve the differences in vortex properties. The objectives of this report are to discuss and summarize the parameters and techniques that could contribute to these differences. The detailed comparisons in this report have helped establish a strong foundation for a PIV data analysis methodology in determining vortex properties.

14. SUBJECT TERMS
HART II, Particle Image Velocimetry (PIV), vortex center, conditional averaging, vortex trajectory method, swirl velocity, vorticity, vortex core radius, centroid, Q criterion, lambda 2, convolution of lambda 2

15. NUMBER OF PAGES
45

16. PRICE CODE

17. SECURITY CLASSIFICATION OF REPORT UNCLASSIFIED	18. SECURITY CLASSIFICATION OF THIS PAGE UNCLASSIFIED	19. SECURITY CLASSIFICATION OF ABSTRACT UNCLASSIFIED	20. LIMITATION OF ABSTRACT UNLIMITED

NSN 7540-01-280-5500

Standard Form 298 (Rev. 2-89)
Prescribed by ANSI Std. Z39-18
298-102

PAGE INTENTIONALLY LEFT BLANK

An Assessment of 3-C PIV Analysis Methodology for HART II Measured Data

Joon W. Lim
Aeroflightdynamics Directorate (AMRDEC)
US Army Research, Development and Engineering Command
Ames Research Center, Moffett Field, California

Berend G. van der Wall
German Aerospace Center (DLR)
Institute of Flight Systems
Braunschweig, Germany

NASA STI Program ... in Profile

Since its founding, NASA has been dedicated to the advancement of aeronautics and space science. The NASA scientific and technical information (STI) program plays a key part in helping NASA maintain this important role.

The NASA STI program operates under the auspices of the Agency Chief Information Officer. It collects, organizes, provides for archiving, and disseminates NASA's STI. The NASA STI program provides access to the NASA Aeronautics and Space Database and its public interface, the NASA Technical Report Server, thus providing one of the largest collections of aeronautical and space science STI in the world. Results are published in both non-NASA channels and by NASA in the NASA STI Report Series, which includes the following report types:

- TECHNICAL PUBLICATION. Reports of completed research or a major significant phase of research that present the results of NASA Programs and include extensive data or theoretical analysis. Includes compilations of significant scientific and technical data and information deemed to be of continuing reference value. NASA counterpart of peer-reviewed formal professional papers but has less stringent limitations on manuscript length and extent of graphic presentations.

- TECHNICAL MEMORANDUM. Scientific and technical findings that are preliminary or of specialized interest, e.g., quick release reports, working papers, and bibliographies that contain minimal annotation. Does not contain extensive analysis.

- CONTRACTOR REPORT. Scientific and technical findings by NASA-sponsored contractors and grantees.

- CONFERENCE PUBLICATION. Collected papers from scientific and technical conferences, symposia, seminars, or other meetings sponsored or co-sponsored by NASA.

- SPECIAL PUBLICATION. Scientific, technical, or historical information from NASA programs, projects, and missions, often concerned with subjects having substantial public interest.

- TECHNICAL TRANSLATION. English-language translations of foreign scientific and technical material pertinent to NASA's mission.

Specialized services also include organizing and publishing research results, distributing specialized research announcements and feeds, providing help desk and personal search support, and enabling data exchange services.

For more information about the NASA STI program, see the following:

- Access the NASA STI program home page at *http://www.sti.nasa.gov*

- E-mail your question via the Internet to help@sti.nasa.gov

- Fax your question to the NASA STI Help Desk at 443-757-5803

- Phone the NASA STI Help Desk at 443-757-5802

- Write to:
  NASA STI Help Desk
  NASA Center for AeroSpace Information
  7115 Standard Drive
  Hanover, MD 21076-1320

NASA/TM-2010-216024
TR-RDMR-AF-10-03

An Assessment of 3-C PIV Analysis Methodology for HART II Measured Data

Joon W. Lim
Aeroflightdynamics Directorate (AMRDEC)
US Army Research, Development and Engineering Command
Ames Research Center, Moffett Field, California

Berend G. van der Wall
German Aerospace Center (DLR)
Institute of Flight Systems
Braunschweig, Germany

July 2010

Acknowledgments

Available from:

NASA Center for AeroSpace Information
7115 Standard Drive
Hanover, MD 21076-1320
443-757-5802

This report is also available in electronic form at

http://

If you need a multiple-column layout, or need to switch to multiple columns at some point in the report, follow these steps (also shown in the instructions file):

1. Ensure that the cursor is at the beginning of a line
2. Select the Insert menu, Break…, and then choose the Continuous section break type
3. Select the Format menu, Columns…, select a preset column layout, and click OK
4. If you want to change back to one column, follow these steps again, selecting the one column layout

Shown below are the text styles available for your report. These styles are also shown in the instructions file, if you want to delete them here, but still be able to see their format.

"Heading 1 STI" – 14 pt. Times New Roman Bold, Centered

This is the —Report Text" style for the body of your report. 11 pt. Times New Roman, flush left, 0.25 first line indent, widow/orphan control on, line spacing single to accommodate inline equations.

"Heading 2 STI" – 12 pt. Times New Roman Bold, Centered

"Heading 3 STI" – 11 pt. Times New Roman Bold Italic, Flush Left

—Heading 4 STI" – Indented bold italic heading with paragraph. Highlight the rest of the paragraph, including the dash, and turn off the bold and italic.

—Heading 5 STI" – Indented italic heading with paragraph. Highlight the rest of the paragraph, including the dash, and turn off the italic.

- This is —Report Text Bullet"

NOMENCLATURE

Q	2nd order tensor (shear) of velocity gradient, s^{-2}
r_c	vortex core radius in the PIV image, m
R	blade radius, m
U	local flow velocity in the horizontal direction, m/sec
V	local flow velocity in the vertical direction, m/sec
W	local flow velocity in the out-of-plane direction, m/sec
α_s	shaft angle, positive aft, degrees
Γ_v	vortex circulation, m^2/s
γ_z	vorticity in the out-of-plane direction, s^{-1}
λ_2	2nd order tensor (strain) of velocity gradient, s^{-2}
ϕ	elastic torsion, degrees
Ω	rotor operating speed, radians/sec
ω_z	angular velocity ($= \gamma_z/2$), s^{-1}
$\sigma_{x, y}$	standard deviations of the vortex centers in the x- or y-direction
θ_x	PIV image rotation in the horizontal axis, degrees
θ_y	PIV image rotation in the vertical axis, degrees
ψ	rotor azimuth, degrees

ACRONYMS

AFDD	Aeroflightdynamics Directorate
BL	Baseline
BVI	Blade Vortex Interaction
CA	Conditional Averaging
DLR	Deutsches Zentrum für Luft-und Raumfahrt, German Aerospace Center
DNW	German-Dutch Wind tunnel
Dpt	Data Point
LLF	Large Low-speed Facility
HART	Higher-harmonic control Aeroacoustic Rotor Test
NASA	National Aeronautics and Space Administration
ONERA	Office National d'Etudes et de Recherches Aerospatiales
PIV	Particle Image Velocimetry
Pos	Position
SA	Simple Averaging
3-C	3-Component

ABSTRACT

Since the completion of the DNW test, HART II partners have put forth significant efforts to derive vortex properties from the measured data. These properties include vortex center, rotation angles of the vortex axis in the PIV measurement plane, maximum vorticity, core radius, and swirl velocity. Differences among the partners' results were found for some of these vortex properties, which required more efforts to assess the physical significance of the differences. This was because the derived vortex properties were an integral of all the sub-processes in the complex PIV data analysis procedure, and more

information was needed to resolve the differences in vortex properties. The objectives of this report are to discuss and summarize the parameters and techniques that could contribute to these differences. The detailed comparisons in this report have helped establish a strong foundation for a PIV data analysis methodology in determining vortex properties.

INTRODUCTION

Particle Image Velocimetry (PIV) measurement data can provide a significant amount of information about vortex core dynamics in a complex flow field. There have been many reports about the PIV data analysis techniques applied to the rotor vortex core properties [1-7], but the techniques have not been standardized in the rotorcraft field, which was partially due to the complexity of the inherent, rotational flow characteristics. Rotor wakes interact with rotor blades and occasionally with returning vortex wakes, which is called Blade-Vortex Interaction (BVI). This BVI phenomenon can be typically seen in descending flight.

One of the difficulties in deriving vortex properties from 3-C PIV measurements is that the plane normal to the vortex axis is unknown a priori. Another difficulty is that the convective velocity of a vortex is also unknown since it is a sum of a free stream velocity and the velocity induced by other vortices. In addition, a vortex is not always rotationally symmetric; often a sheet of trailed vortices is found spiraling around a vortex.

This report describes the efforts of an internationally-joint HART II team for extensive analyses of the PIV database that was acquired during a wind tunnel test of the HART II rotor. A brief description of the PIV database is also provided, and the techniques for deriving vortex properties such as vortex center, rotation angle of the vortex axis, maximum vorticity, core radius, and swirl velocity are followed. Differences in resulting vortex properties among the partners are addressed and discussed. Specific findings from this study are provided in the conclusions.

HART II 3-C PIV DATA

In 2001, an international cooperative test, called the Higher-Harmonic-Control Aeroacoustic Rotor Test (HART II) was conducted by the US Army Aeroflightdynamics Directorate (AFDD), Deutsches Zentrum für Luft-und Raumfahrt (German Aerospace Center, DLR), Duits-Nederlandse Windtunnel (German-Dutch Wind Tunnel, DNW), National Aeronautics and Space Administration (NASA), and the Office National d'Etudes et de Recherches Aerospatiales (Onera) at the large low-speed facility (LLF) of the DNW wind tunnel. Primary objectives of the test were to measure rotor wake information extensively using 3-component (3-C) PIV, blade surface pressure distributions, blade deformations, and acoustic signatures [8-10].

The rotor was a 40% Mach-scaled, hingeless Bo105 main rotor (HART II), and had a precone of 2.5 degrees at the hub, operating at 1041 rpm. The blade was 2 meters long with -8 degrees twist, and consisted of a NACA-23012 airfoil section with a trailing edge tab. The chord length was 0.121 meters. The hover tip speed was 218 m/s with a tip Mach number of 0.64. The rotor shaft angle in the test was 5.3 degrees aft.

Figure 1 shows the HART II 3-C PIV setup that included three double-pulsed Nd:YAG lasers and four digital cameras mounted onto a remote-controlled traverse system. This traverse system was located outside of the shear layer in the open jet configuration and moved in the direction of flow. Four cameras on the traverse system were used to collect 3-C PIV data. One pair of cameras used 100mm lenses for a larger observation area (DNW measurement window) and the other camera pair used 300mm lenses to investigate the tip vortex with high spatial resolution (DLR measurement window).

The PIV measurement plane coordinate system has the positive x-axis to the right direction, the positive y-axis up and the positive z-axis out of plane. The rotor hub coordinate system is aligned with the

rotor shaft, such that the positive x is toward the tail boom, the positive y is toward the right wing, and the positive z is upward along the shaft. The wind tunnel coordinate system is defined as the inertial frame without considering a shaft tilt: the positive x upstream, the positive y to the right (pilot's view), and the positive z down.

Figure 2 shows the location and orientation of the PIV measurement planes for the HART II test. To avoid interference of the blades with the measurement plane, the reference blade was located alternatively at an azimuth of 20° or 70°. In each measurement plane (black line segment), one hundred individual PIV images were obtained, and the numerals represent the identification number of each PIV measurement position. The measurement planes were oriented at an angle of 149.35^o for the advancing side and 30.06^o for the retreating side with respect to the positive hub x-axis.

Figure 3 shows an individual image for Dpt 995 (position 21), taken by the camera. The upper image (0.45m x 0.38m) is the global view taken from the DNW camera with the apparent center of swirl motion (vortex center) in the flow field. The close-up view image (0.15m x 0.13m) from the DLR camera shows the indicated area of the vortex with a higher resolution. However, the high resolution image does not indicate a clear swirl motion.

The velocities (U, V and W) and the vorticity for image #1 at the position 17 are shown in Fig. 4. The vorticity, γ_z was derived using the relation:

$$\gamma_z = 2\,\omega_z = \mathbf{k}\,\cdot\,(\text{curl } \mathbf{V}) = \frac{\partial V}{\partial x} - \frac{\partial U}{\partial y} \tag{1}$$

where ω_z is the angular velocity and $\mathbf{V} = (U, V, W)$. In the figure, the peak vorticity and noise of the measurement are easily observed. The noise may result from natural turbulence and unsteadiness of the flow field, and the vortex center could be affected by rotor test stand vibration, camera support vibration and other unknown resources.

VORTEX CENTER AND CONDITIONAL AVERAGING

Averaging a large number of velocity vector fields will reduce the noise inherent in an individual image. It is straightforward to overlay all of the individual velocity fields in the PIV images and then to average them to a single velocity field. This is called simple averaging (SA) technique and works well when the vortex centers are mostly collocated from one image to another. In the test setup, the rotor model stand was attached to the tunnel sting. The sting and the camera supports were slightly vibrating at low frequencies due to elasticity. The test rig vibrations were transferred to the blades, which resulted in scattering of the vortex centers between individual PIV images. In addition, natural instabilities of helical vortex systems added vortex wandering with the vortex age. This situation makes it necessary to conduct a conditional averaging (CA) technique in order to prevent smearing of the vortex which would occur if the SA technique is employed. The details of a conditional averaging technique are given in Ref. [11]. Figure 5 shows the procedure for conditional averaging of velocity fields, which is briefly given as follows:

1) Specify the sense of rotation of the vortex under investigation, since the vortices in the opposite rotation could be in the same image.
2) Identify the vortex center location in each PIV image using a sub-grid.
3) Compute the standard deviation of vortex centers for all 100 PIV images.
4) Within a user-specified Z score (Z ≈ 1.5) select 80-95 individual images (geometric outlier removal). Re-compute the mean vortex center position based on selected PIV images. Note that Z score is the sample score non-dimensionalized with a standard deviation.
5) Perform a conditional averaging by collocating selected images with individually computed vortex centers. The vortex center of each image does not necessarily lie on a grid point, which

requires re-meshing of the individual images and then interpolating their velocities in the re-meshed images.

A vortex can be defined using a various form of velocity tensors. We consider here four different velocity gradient tensors for identification of a vortex: vorticity γ_z, Q criterion, λ_2 and convolution of λ_2 [11-12]. The first order tensor, vorticity, is widely used in identifying a vortex. Higher order tensors are understood to display a clearer image of a vortex than the lower order tensor. The second order tensors include Q criterion, λ_2 and convolution of λ_2. The first two definitions are similar to each other, and their explicit expressions for the two-dimensional velocity field are given as follows [11, 13-14]:

$$\lambda_2 = \frac{1}{2}\left[\left(\frac{\partial U}{\partial x}\right)^2 + \left(\frac{\partial V}{\partial y}\right)^2\right] + \frac{\partial V}{\partial x}\frac{\partial U}{\partial y}$$

$$Q = \frac{1}{4}\left(\frac{\partial U}{\partial x} + \frac{\partial V}{\partial y}\right)^2 - \frac{\partial U}{\partial x}\frac{\partial V}{\partial y} + \frac{\partial V}{\partial x}\frac{\partial U}{\partial y} = \frac{1}{2}\cdot\left[\lambda_2 - \frac{\partial U}{\partial x}\frac{\partial V}{\partial y} + \frac{\partial V}{\partial x}\frac{\partial U}{\partial y}\right]$$

(2)

Note that vorticity (the first order tensor, γ_z) provides information on the sense of rotation via its sign, but the second order tensors (Q and λ_2) do not provide this information — the sign of their peak values is independent of the sense of rotation. The convolution of λ_2 maps the λ_2 distribution into a bell-shaped normal distribution, S using a normal shape function, F as

$$S(i,j) = \frac{1}{c}\sum_{j=-m}^{m}\sum_{i=-l}^{l}\lambda_2(i+l,j+m)\cdot F(l,m)$$

$$\text{where} \quad F(l,m) = e^{-g\cdot r^2}$$

(3)

$$c = \sum_{j=-m}^{m}\sum_{i=-l}^{l}F(l,m)$$

$$r(l,m)^2 = \left[x(l,m) - x(0,0)\right]^2 + \left[y(l,m) - y(0,0)\right]^2$$

The newly mapped scalar field, S (convoluted flow field) is computed by superposition of a normal shape function, F, over a sub-grid consisting of $2l+1$ by $2m+1$ grid points. Typically, a value of 7 is used for l and m, and the grid point $(0, 0)$ denotes the peak location of the shape function, F. The factor c is a scale factor to normalize the convoluted flow field. For example, the convoluted flow field will result in a value of unity if $\lambda_2 = 1$ everywhere in the sub-grid enclosed by $2l+1$ by $2m+1$ grid points. The factor g, which is a shape factor to F for a bell-shaped distribution, depends on the non-dimensional grid resolution, Δx or Δy. In this report, $g = (\Delta x/0.003)^2$ is used. Note that convolution can be taken with any of the first or second order tensors instead of λ_2 in the above equation.

The vortex center of an individual velocity field can be identified using various vortex identification methods. A weighted mean of velocity gradient tensors is computed for each individual image. A weighted mean of vorticity is called the vorticity —centroid", and is defined as

$$\bar{x} = \frac{\sum x_i \cdot \gamma_{z,i}}{\sum \gamma_{z,i}}, \quad \bar{y} = \frac{\sum y_i \cdot \gamma_{z,i}}{\sum \gamma_{z,i}}$$

(4)

A summation is performed over the sub-grid, which is a small neighboring region of a peak vorticity. Typically, we define this sub-grid as the regions including the top 10% of the peak vorticity. A vortex center using the second-order velocity gradient tensors or a convolution of velocity gradient tensors can be computed in a similar manner.

After the vortex center is computed for each of the PIV images, we select 80-95 images for averaging in order to remove outliers. This corresponds to a Z score of 1.28-1.96, which was recommended by HART II partners based on their collective experience. The vortices with their centers being outside of a user-defined Z score are considered geometric outliers. Alternatively, the vortices with their peak value of vorticity, Q or λ_2 outside of the specified threshold are considered strength outliers.

Considering a normally distributed sample, the standard deviation of vortex center is defined in the x- and y-directions as

$$\sigma_x = \sqrt{\frac{\sum (x_i - \bar{x})^2}{N-1}}, \quad \sigma_y = \sqrt{\frac{\sum (y_i - \bar{y})^2}{N-1}} \tag{5}$$

The x_i and y_i are the vortex center in the x- and y-directions for an individual PIV image, N is the sample size and the bar indicates the mean value. A distribution of the sample data can be eccentric in either the x- or y-direction. Therefore, a circular standard deviation (i.e., $\sigma_r = \sqrt{\sigma_x^2 + \sigma_y^2}$) may not be sufficient to standardize the two dimensional, normal distribution. So, we define here a circular Z score for an isotropic scaling.

$$X = \frac{x_i - \bar{x}}{\sigma_x}, \quad Y = \frac{y_i - \bar{x}}{\sigma_y}, \quad Z = \sqrt{X^2 + Y^2} \tag{6}$$

For conditional averaging, each selected PIV image is collocated with its vortex center as shown in Fig. 5, and a new vortex center is computed only with the selected 80-95 individual PIV images. The conditional averaging is a mandatory process for the analysis of vortex properties in the HART II PIV database [11].

ROTATION OF AVERAGED VELOCITY FIELD

Tung et al. [15] presented calculations of vortex core velocities using the vortex trajectory method. Burley et al. [16] presented two different methods to determine the orientation of the vortex core with respect to the PIV measurement plane. Specifically, one method uses the axial flow within the vortex core and the other uses the tangential (or spin) velocity within the vortex core to define the orientation. In this report, a simple geometry-based vortex trajectory method is used to determine the convective velocity and the orientation of vortex core axis.

In the vortex trajectory method, an averaged velocity field is rotated using a transformation matrix. The apparent vortex trajectory is constructed using the vortex centers derived from the averaged measured velocity fields, based on the assumption that a vortex trajectory is normal to the vortex core axis or the PIV measurement plane. This vortex trajectory method was employed by AFDD using the kinematics of Euler rotation by means of a vector dyadic [15]. The method computes Euler rotation angles of the vortex axis, taking into account the effect of deformation of the vortex trajectory. Later, an alternative approach was used by DLR using the direction cosines computed from the estimated vortex trajectory polynomials that were constructed from neighboring PIV measurement plane origins [17].

AFDD Vortex Trajectory Method

For any three adjacent vortex positions P_1, P_2 and P_3, one can fit a circular arc through these points. These vortex positions are the vortex centers derived from the averaged velocity fields. In Fig. 6, the normal vector ($\mathbf{B_3}$) is defined as the unit vector parallel to the vector connecting the two positions (P_1 and P_3), crossing at the position P_2. This normal vector and the in-plane vector connecting the positions P_1 and P_2 ($\overrightarrow{P_1P_2}$) form the vortex trajectory plane, and the cross product of these two vectors gives the

vertical vector (**B₂**) at the position P_2. Again, the cross product of the vertical vector and the normal vector at the position P_2 gives a bi-normal vector (**B₁**). Thus, the rotated PIV plane, which is normal to the vortex trajectory, contains the bi-normal vector in the x direction (**B₁**) and the vertical vector in the y direction (**B₂**). The mathematical expressions for these three vectors are described in terms of the positions, P_1, P_2 and P_3 as:

$$\mathbf{B}_3 = \frac{\overrightarrow{P_1P_3}}{\left\|\overrightarrow{P_1P_3}\right\|}, \quad \mathbf{B}_2 = \mathbf{B}_3 \otimes \frac{\overrightarrow{P_1P_2}}{\left\|\overrightarrow{P_1P_2}\right\|}, \quad \mathbf{B}_1 = \mathbf{B}_2 \otimes \mathbf{B}_3 \tag{7}$$

Note that determination of the normal vector (**B₃**) may introduce a large error if the position P_2 is not the mid-point of a circular arc connecting the three vortex positions (P_1, P_2, P_3).

Rotation angles can be found from kinematics of Euler rotation. A transformation matrix of an unrotated PIV image to a rotated one is determined from Euler rotation sequence. The rotation angles are computed using a transformation matrix in the following dyadic relation:

$$\mathbf{B}_i = \mathbf{T}_{xyz}^{BA} \cdot \mathbf{A}_j = T_{xyz}^{BA}\big|_{ij} A_j, \quad \forall \; i,j = 1,2,3 \; \text{ where } \; \mathbf{T}_{xyz}^{BA} = \mathbf{B}_i \cdot \mathbf{A}_j = B_i A_j \tag{8}$$

where **A** and **B** are the unit vectors in the unrotated and rotated planes, respectively. The rotation tensor $\mathbf{T}_{xyz}^{BA}$ is a transformation matrix (dyadic tensor) containing all three rotation angles in nature with a rotation sequence about the z-, y-, and then x-axes. To eliminate unnecessary z-rotation in the rotated PIV image, one could take the inverse z transformation such that

$$\mathbf{T}_{xy}^{BA} = \mathbf{T}_{xyz}^{BA} \cdot \mathbf{T}_{z^{-1}}^{BA} \tag{9}$$

The rotation angle about the z-axis is computed using $\mathbf{T}_{xyz}^{BA}$ by the relation, $\theta_z = \tan^{-1}(T_{12}/T_{11})$. Thus, the transformation matrix having a rotation about the y-axis and then the x-axis, is given by

$$\mathbf{T}_{xy}^{BA} = \begin{bmatrix} cy & 0 & -sy \\ sx \cdot sy & cx & sx \cdot cy \\ cx \cdot sy & -sx & cx \cdot cy \end{bmatrix} \tag{10}$$

The finite rotation angles (horizontal and vertical) are computed by

$$\theta_x = \tan^{-1}\left(\frac{T_{23}}{T_{33}}\right), \quad \theta_y = -\sin^{-1}\left(T_{13}\right) \tag{11}$$

This method requires three vortex measurement positions to compute the associated vectors. When actual measurement is not made at three points along the vortex trajectory, there is not enough information to compute the vortex trajectory. In such cases, the vortex positions could be estimated using the available PIV measurement plane positions, ignoring deformation of the vortex trajectories.

DLR Vortex Trajectory Method

This method estimates the vortex trajectory by constructing polynomials based on PIV measurement plane positions, based on the assumed vortex centers as the origin of the PIV measurement plane [17]. The direction cosines are computed from the estimated vortex trajectory polynomials in the

wind tunnel coordinate system, and the corresponding direction cosine angles are inversely computed by the following relations:

$$\gamma_{x,hub} = \tan^{-1}\left(\frac{\Delta y_{hub}}{-\Delta x_{hub}} \right), \text{ and } \gamma_{y,hub} = \tan^{-1}\left(\frac{-\Delta x_{hub}}{\Delta z_{hub}} \right) \tag{12}$$

These angles are transformed back into the PIV measurement plane coordinate system, where the sense of rotation is defined as follows:

$$\vartheta_x = \begin{cases} -\gamma_{x,hub}, & \forall \text{ advancing side} \\ \gamma_{x,hub}, & \forall \text{ retreating side} \end{cases}, \quad \vartheta_y = \begin{cases} -\gamma_{y,hub} + 30^{\circ}, & \forall \text{ advancing side} \\ \gamma_{y,hub} - 30^{\circ}, & \forall \text{ retreating side} \end{cases} \tag{13}$$

Note that these angles are direction cosine angles and can be converted into Euler angles using a coordinate transformation matrix.

The AFDD and DLR vortex trajectory methods provide a good estimate for rotation angles of a PIV image, and quantitative comparison will be given in a later section. There are the cases having the unbalanced (non-concentric) contours of the cross flow field surrounding the vortex center, which may require an additional adjustment in the rotation of the velocity field. In such cases, we incrementally rotate the unbalanced cross flow field until it becomes concentric. When the cross flow field is concentric around the vortex center, the vorticity field also becomes concentric under the ideal situation [11]. In reality, interactions with shear layers, turbulence or other unsteady behaviors will make the contours to be non-concentric.

COMPUTATION OF GRADIENTS

All flow field tensors such as vorticity, Q and λ_2, are based on the gradients of the velocity field, i.e. $\partial V/\partial x$, $\partial U/\partial y$, $\partial V/\partial y$ and $\partial U/\partial x$. Various numerical schemes are available to compute these gradients. The most commonly accepted scheme is the 2nd-order-accurate central difference scheme in one dimension. More accurate schemes are available, such as the 3rd-order-accurate Richardson extrapolation. These schemes are given as follows:

central difference: $\quad \left.\dfrac{\partial V}{\partial x}\right|_{i,j} = \dfrac{V_{i+1,j} - V_{i-1,j}}{2\,\Delta x} + O(\Delta x^2)$

$$\tag{14}$$

Richardson extrapolation: $\left.\dfrac{\partial V}{\partial x}\right|_{i,j} = \dfrac{-V_{i+2,j} + 8V_{i+1,j} - 8V_{i-1,j} + V_{i-2,j}}{12\,\Delta x} + O(\Delta x^3)$

An alternative numerical scheme is to include two-dimensional dependency of the velocity fields in the PIV measurement planes. Reference [18] provides a derivation based on circulation around a point of interest. The vorticity is expressed using Stokes' theorem as follows:

$$\gamma_{z,ij} = \left.\frac{\partial V}{\partial x}\right|_{i,j} - \left.\frac{\partial U}{\partial y}\right|_{i,j} = \frac{\Gamma_{ij}}{A_{ij}} \quad \text{where } \Gamma_{ij} = \int \gamma \cdot d\mathbf{S} = \oint \mathbf{V} \cdot d\mathbf{l} \tag{15}$$

where A_{ij} is the area enclosed by the grid points, $(i-1,j-1)$, $(i+1,j-1)$, $(i+1,j+1)$, and $(i-1,j+1)$ around the point of interest. This integration takes into account the velocity data from eight surrounding grid points. For equally spaced grid points around the point (i,j), the gradients $\partial V/\partial x$ and $\partial U/\partial y$ are:

$$\left.\frac{\partial V}{\partial x}\right|_{i,j} = \frac{V_{i+1,j-1} + 2V_{i+1,j} + V_{i+1,j+1} - V_{i-1,j-1} - 2V_{i-1,j} - V_{i-1,j+1}}{8\,\Delta x}$$

$$\left.\frac{\partial U}{\partial y}\right|_{i,j} = \frac{U_{i-1,j+1} + 2U_{i,j+1} + U_{i+1,j+1} - U_{i-1,j-1} - 2U_{i,j-1} - U_{i+1,j-1}}{8\,\Delta y}$$

(16)

Note that U and V are the velocities in the x- and y-directions, respectively. This approach is equivalent to applying the central difference scheme to a smoothed 3x3 kernel velocity field, and the uncertainty in the vorticity estimate with this approach is therefore expected to decrease. Other gradients such as shear strain can be computed in a similar fashion. It is noted that the robustness of this approach over the central difference or Richardson's extrapolation is described in Ref. [18].

VATISTAS MODEL

Tip vortices often interact with other flow structures including shear layers, turbulence and vortices shed from other blades. A characterization of a vortex core model can be made with a curve-fit to a swirl (tangential) velocity profile of a vortex [11, 19]. A simple model is the Rankine vortex, which models the core as a solid body. The Oseen-Lamb model is expressed in terms of the exponential decay function as a simplified solution of the Navier-Stokes equation [20]:

$$V_\theta = \frac{\Gamma_v}{2\pi r_c} \cdot \frac{1 - e^{-\alpha \cdot \rho^2}}{\rho} \qquad \text{where } \rho = \frac{r}{r_c}$$

(17)

Γ_v is the vortex circulation, and r_c is the vortex core radius. The coefficient α depends on the kinematic viscosity and vortex age, which can be set as 1.25643 [19]. A more general mathematical expression for a swirl velocity profile is given by Vatistas et al. [21] as

$$V_\theta = \frac{\Gamma_v}{2\pi r_c} \cdot \frac{\rho}{(1 + \rho^{2n})^{1/n}}$$

(18)

At the vortex core radius ($\rho = 1$), the maximum swirl velocity should satisfy the relation,

$$V_{\theta,\max} = \frac{\Gamma_v}{2\pi r_c} \cdot 2^{-1/n}$$

(19)

Therefore, the total circulation Γ_∞ of a potential vortex is determined such that

$$\Gamma_\infty = 2\pi r_c \cdot V_{\theta,\max} = \Gamma_v \cdot 2^{-1/n}$$

(20)

Note that the Scully core model, which is widely used in the rotorcraft field, is identical to the Vatistas model with $n = 1$. The Rankine vortex model is obtained as $n \to \infty$, and the Lamb-Oseen model is closely approximated when n = 2 [19].

8

RESULTS AND DISCUSSION

The PIV analysis results collected from HART II partners were presented by the DLR [22]. Sample comparisons of the derived vortex core properties for the baseline case are presented in Fig. 7. Vortex positions, rotation angles, peak vorticity, core radius and peak swirl velocity are shown. Comparisons are made in the longitudinal cutting plane of $y/R = 0.7$ on the advancing side. Small-to-large differences among the partners' results were found, and assessing the physical significance of these differences was difficult. In fact, the findings were not sufficient to resolve the differences. This report will discuss and summarize the parameters and techniques which could contribute to these differences.

Discussion about the simple averaging technique [11, 13] is not included in this report since HART II partners have agreed that conditional averaging is required for HART II PIV analysis. The HART II partners have also agreed to use the PIV measured data in 24 pixels x 24 pixels (interrogation window size with 50% overlap) due to more availability of the data in the HART II database. In this report, only the data from the DLR measurement window will be presented. The cameras for a close-up view (DLR window) had a resolution of 1280 x 1024 pixels, the exposure time of an individual PIV image was about 120 μs, and the time delay between the two PIV images was mainly 17 μs.

Conditional Averaging

At each PIV measurement position, one hundred individual images are available. A young vortex, which sheds from the preceding blade at an azimuth of 135.6° (refer to Fig. 2a), quickly reaches position 17 (Dpt 1003) at a wake age of 25.3°, and is accompanied by a strong shear layer generated along the blade trailing edge. For a lightly loaded rotor, the vorticity strength of a shear layer has a similar magnitude to the tip vortex as in this case. For a highly loaded rotor as seen on the retreating side or in hover, the vorticity strength of a shear layer becomes less significant compared to the tip vortex.

After passing the position 17, the young vortex continuously travels downstream. When it reaches the first quadrant of the rotor disk, the vortex is already grown to a fully-developed vortex and encounters significant blade-vortex interactions (BVI) with following blades, which is a typical phenomenon in descending flight. A good example of a fully grown vortex is the one at position 22 (Dpt 998), which is at a wake age of 425.3°. Figure 8 shows typical (unrotated) vorticity maps for positions 17 and 22. The vorticity was non-dimensionalzed with the rotor operating speed. A fully grown vortex at the position 22 displays its strength more diffused than a young vortex at the position 17.

The vortex centers of one hundred individual images are plotted in Fig. 9 for position 17 (Dpt 1003) of the baseline case. AFDD used a centroid for the center identification while DLR used convolution of λ_2. The centroid method displays individual vortex centers largely collocated with some scatter, while the convolution of λ_2 method results in much less scatter.

Figure 10 compares conditionally averaged vortex centers for position 17 (Dpt 1003). The vortex centers computed using a centroid (AFDD), Q criterion (Onera), and λ_2 and convolution of λ_2 (DLR) are almost collocated, with difference of 0.02-0.04% R (0.36-0.61% c). A tabulated comparison of the vortex properties for position 17 is given in Table 1a, which includes the maximum vorticity, vortex centers and their standard deviation. Note that 1% of the blade radius is equivalent to 16.5% of the blade chord length.

Differences in vortex properties among various methods are given in Table 1b. The reference value was taken from the centroid result. The differences of maximum vorticities fall within 7% of the rotor speed. The vortex centers that were derived using a centroid, Q criterion and λ_2 show good agreement, but the vortex center from convolution of λ_2 is different from the other methods by about 0.3-0.5% of the chord.

The vorticity maps, computed using a centroid, Q criterion, λ_2 and convolution of λ_2, are shown in Fig. 11, exhibiting a strong shear layer. This shear layer, resulting from airfoil thickness, includes the effects of the boundary layer (mainly in the cross-flow component) as well as the radial circulation

distribution (vorticity). The vorticity and shear layer contours of the four methods appear almost identical to each other, except for the value of the maximum vorticity. Figure 12 shows the same comparison but with the first- and second-order velocity gradient tensors, and demonstrates that the level of difficulty in visual identification of vortex center significantly reduces with the second-order tensors. Note that the coordinate system of the contour using Q criterion was rearranged at the vortex center. Although all the second order tensors (Q criterion, λ_2 and convolution of λ_2) display a cleaner image of the vortex core than the first-order tensor, the accuracy in the vortex center location does not depend on the order of the tensor — at least within this example — as seen in Table 1.

The conditionally averaged vortex centers at position 22 are compared in Table 2. The centroid results are used as a reference. The vortex center using Q criterion differs largely by 2.0-3.3% of the chord. Considering vortex core radius to be 4-15% of the chord for a typical rotor tip vortex, this difference is not trivial.

Number of Individual PIV Images

When inspecting each individual PIV images, some images were found to be too diffused or blurry. In most cases, these images were identified outliers. A typical characteristic of these outlier images is that the vortex core image is diffused and the vortex center is away from the mean vortex center. Figure 9 shows the vortex centers of all 100 individual images using the centroid and the convolution of λ_2. Outlier images were eliminated in conditional averaging (geometric outlier removal). Selecting good images from the population of 100 images is controlled by a Z score of the normally distributed vortex centers. Choosing the images with a 95% confidence level corresponds to a Z score of 1.96, and HART II partners agreed to use about 80-95 images, corresponding to Z = 1.28-1.96.

Table 3 shows a relationship between a Z score and the number of the PIV images selected. As expected, the maximum vorticity rapidly decreases when more images are included for averaging. The corresponding vorticity maps are shown for position 17 in Fig. 13. The vortex contours are almost unchanged with a variation of Z scores, but the peak vorticity values (hot spot) are moderately changed. With 39 images (Z=0.5), the peak vorticity increases by 16% from the vorticity with 89 images.

In addition to this geometric-position-based elimination of outliers, one can alternatively consider dealing with vortex strength (strength outlier removal) by analyzing the peak vorticity, peak Q, peak λ_2 or the peak value of the convolution with any of those inside a vortex core. For example, one can eliminate the images having unusually lower vortex strength by defining a threshold (or Z score) below the mean. The reasoning is that blade-vortex-interaction noise is dominated by the strongest interactions and a proper averaging should thus retain the strongest vortices for analysis of their properties. The number of the images eliminated by this method is similar to the number with the geometric outlier removal, and thus the number of remaining images with the strength outlier removal is typically in the range of 80-95. However, in cases where the vortex of interest is close to another one having the opposite sense of rotation (dual vortices), the number of images may drop down significantly, and an automatic procedure for robust identification of the images requires more complicated sub-processes.

Sub-grid in Vortex Center Identification

A vorticity field typically displays a hot spot where a strong vortex lies, and so it is not difficult to visually identify a vortex center. An automatic identification of a vortex center using a computer program, though more consistent and objective, is not as straightforward as a visual identification. It is more difficult to identify a vortex center containing some noise and a shear layer. Figure 14 shows a perspective view of the vorticity map of image #3 at position 17. A sharp peak of a vortex is accompanied by a series of moderate peaks from a shear layer.

The PIV measurement data are provided on a grid, and the scalar values (first and second order tensors) are computed on the grid to identify a vortex center. The physical vortex center, however, is not

confined to any resolution represented by this grid, and can be anywhere between the grid points. For this reason, re-meshing of the grid points by interpolation is required.

A vortex center in the vorticity map is determined by first computing the vortex strength (γ_z, λ_2, Q or convolution of λ_2) on the grid and then searching for the maximum vortex strength to determine the vortex center. A sub-grid is a small neighboring region surrounding peak vorticities, and the neighboring region is defined by a specified threshold in terms of the maximum vortex strength. Figure 14 shows sub-grids with the top 10% and 40% of the vorticity peak, and the latter case (top 40%) displays two sub-grids which would result in a large shift of the vortex center.

Figure 15 shows the vortex centers of image #3 at position 17 with sub-grids defined using the top 10% to 50% of the peak vorticity. Note that the grid resolution in the PIV data was 1.25% of the chord (= 0.0756% R) in both the x- and y-directions. The sub-grid with the top 50% results in a vortex center shifted 15% chord away from the vortex center computed with the top 10%. As observed, the sub-grid size is sensitive in determining a vortex center. The question remains about what sub-grid size is adequate for determining the vortex center. We recommend using the top 10% of the maximum strength of a vortex (γ_z, λ_2, Q or convolution of λ_2) for a sub-grid definition. Note that this sub-grid is used only for identifying the vortex centers in each individual image.

Figure 16 shows the perspective and top views of λ_2 and convolution of λ_2 of image #3 at position 17 (Dpt 1003). As compared to the vorticity using a centroid method in Fig. 14, the perspective view of λ_2 (Fig. 16a) seems slightly cleaner. But, the views of the convolution of λ_2 display less noisy even when compared with the same 2nd-order tensor, λ_2.

Conditional Averaging Using a Subset of the PIV Database

The PIV data analysis is an integral of all the sub-level processes in conditional averaging with the various numerical differentiation schemes for computing velocity gradients, which affect the first- and second-order tensor data. Establishing thresholds for removing outliers is another sub-level process followed by applying various vortex center identification methods. The differences between HART II partners' results (Fig. 7) originated from each of the sub-level processes. Due to the large size of the PIV database, data analysis became very complex and quantifying these differences at each sub-process level became challenging. To help this situation, we attempted a conditional averaging with a subset of the data, so that a few PIV images were used instead of all 100 images.

For this exercise, two PIV positions were selected in the longitudinal plane of y/R = 0.7 on the advancing side: position 17 (Dpt 1003) and position 22 (Dpt 998). Two individual images were used for position 17 and three images for position 22. Conditionally averaged results with these images are compared for the two positions 17 and 22.

a) Case 1: Pos 17 (Dpt 1003)

Figure 17 shows the first 16 individual PIV images at position 17 of the baseline. Among these 16 images, images #1 and #3 are selected for this exercise. Figure 18 shows a comparison of vortex properties for image #1 as calculated by the HART II partners. The figure shows a strong vortex (hot spot), accompanied by a moderately strong shear layer. The maximum vorticity is much higher than the conditionally averaged value using all the images (see Table 1). The label, _A' in the contour stands for AFDD, _D' for DLR, and _O' for Onera. In a large window (left image), vortex centers are collocated almost to each other, and so this image is enlarged by roughly 25 times (right image). Note that one grid spacing in this enlarged image is equal to 1.25% of the chord (= 0.0756% R), and 1% of the radius (% R) equals to 16.5% of the chord. The maximum vorticity difference (Δ_{max}) between different methods is small, and the difference in the circular vortex center ($\Delta r_v = \sqrt{\Delta x_v^2 + \Delta y_v^2}$) is 0.06% R (= 0.99% c), as shown in Table 4a.

A similar comparison was made for image #3 in Fig. 19 and Table 4b. This image appears slightly fuzzy. Computed vortex properties, such as vorticity as well as vortex center, are almost identical to each other when using the centroid and Q criterion methods. The vorticity by the convolution of λ_2 is also similar to the values by other methods, but its vortex center shifts to the x-direction by about 0.08% R (= 1.36% c).

Finally, both images were used for conditional averaging. The vortex properties with images #1 and #3 are compared in Fig. 20 and Table 4c-4d. The vorticity by the convolution of λ_2 is 10% higher than the value using a centroid or Q criterion. The vortex center by the convolution of λ_2 differs from the centroid method result by 0.03% R (= 0.50% c).

b) Case 2: Pos 22 (Dpt 998)

Figure 21 shows first 16 individual images at position 22 of the baseline. Images #2, #3 and #8 are used for conditional averaging. The images #2 and #3 show a clear hot spot and the image #8 seems slightly fuzzy. The vortex at this position is fully grown, its vortex strength diffused, and the flow field seems relatively noisy.

Vortex properties are derived using conditional averaging by the centroid and convolution of λ_2 methods shown in Fig. 22 and Table 5. The peak vorticity at the position 22 is substantially less than the peak at the position 17. The circular vortex center is different by 0.054% R (= 0.89% c) between the two methods. Note that a fuzziness of the vortex image in this figure is seen typically from older vortices.

Rotation Angles for an Averaged Image

The PIV measurement plane is not generally normal to the vortex trajectory due to pre-setting the orientation of the measurement plane prior to the test. Since an accurate analysis of the vortex core can be made only in the vortex axis, the rotation angles from the measurement plane to the vortex axis should be accurately identified. In this study, these rotation angles were defined in terms of Euler angles with a sequence of the y-x rotation, or direction cosine angles. Ideally, the resulting vortex image will be normal to the vortex trajectory after rotation.

As a general hypothesis, every vortex in an individual PIV image is assumed to have the same inclination of the vortex axis with respect to the measurement plane, though the vortex axis orientation may vary in each individual image. During the PIV analysis exercise among the HART II partners, the discussion evolved whether individual images should be rotated prior to conditional averaging or not, and the conclusion was that this would introduce additional complication and uncertainties without having significant benefits. After the rotation of the velocity field, the meshes in the rotated image are no longer orthogonal and thus data interpolation on the rotated grid of the individual images becomes more complicated. In addition, the analysis of rotation angles for each individual is repeated over the number of individual images. Reference [11] showed, using hover data, that averaging of individual rotation angles was in agreement within one degree tolerance despite a standard deviation of about four degrees, and this difference is considered negligible. Therefore, the conditionally averaged velocity field will be used in the present work.

Figure 23 shows the contours of vorticity (γ/Ω) and cross flow ($V_{zv}/\Omega R$) before and after rotation. Note that the cross flow velocity was filtered out by the velocity at the vortex center. The conditionally averaged image was generated using a centroid method with images #2, #3 and #8 at position 22. The rotation angles were found to 6.3^{o} and -34.3^{o}, respectively, in the x- and y-axes of the PIV measurement plane. The peak vorticity of the unrotated image was 24.40, and that of the rotated image was 24.41. Small differences are observed in both peak values and the contour patterns, which forces to preclude using the vorticity map for judging the quality of rotation angles. On the contrary, the cross flow velocity field shows a relatively good quality of concentric contour after rotation. Therefore, the cross-flow velocity field is considered a primary indicator for an identification of rotation angles in this report. Though the resulting image is a projection of the measured data at a view angle parallel to the vortex axis,

it is assumed that the flow field may not be significantly different within the volume covered by the z-coordinate of the image after rotation. The projection can be also assumed as being measured in the plane normal to the vortex axis, and thus an analysis of vortex properties may be allowed within this projected data field.

Figure 24 compares two rotation angles (horizontal and vertical), at position 22, derived using the centroid (AFDD) and the convolution of λ_2 (DLR). Larger differences in the rotation angles between the two methods are found from image #8. This result is expected since image #8 is fuzzy compared with the other two images and so more difficult to accurately identify the vortex properties. The rotation angles after being conditionally averaged (ca) are shown in the figure. Interestingly the difference of the rotation angles from the averaged image is less than that from the single image #8, and a similar example is found in Ref. [11]. In Table 6, the difference in the rotation angles between the two methods is about 3° or less with a conditional average, but the difference increases to 6° to 12° when the rotation angles are compared between individual images. Derived rotation angles using all 100 images (see Fig. 7), are given in Table 7 for positions 17 and 22. Note that after rotation into the vortex axis system, the resulting grid is no longer orthogonal and skewed instead. Care must be taken when derivatives such as $\partial V/\partial x$ are computed, since the data must be properly interpolated.

Swirl Velocity

An accurately rotated vorticity or velocity field in the PIV image displays a concentric contour around the vortex center, provided that the vortex is rotationally symmetric. This concentric contour can be distorted due to interactions with other vortices, shear layers, or turbulence. From the rotated, averaged velocity field, a swirl velocity can be reconstructed in two steps. First, tangential velocities are collected from the cutting axes — the straight lines in the radial direction from a vortex core. The direction of the cutting axes can be to the right, up, left, down and in between, and this process generates multiple tangential velocity profiles. Secondly, by taking an algebraic averaging of these velocity profiles, the desired tangential velocity profile is obtained.

As an alternative approach, all individual images can be separately analyzed instead of a single averaged image. Collecting individual velocity profiles provides a tangential velocity ―loud‖, from which an averaged tangential velocity profile can be computed. The outlier removal methodology can be applied to reduce the bandwidth of the cloud before averaging (DLR approach).

Figure 25 shows the vorticity map and tangential velocities of the conditionally averaged image at position 17 using the centroid method. Images #1 and #3 were used for averaging. The cutting axis azimuths are shown on the vorticity map as an example, and the associated tangential (swirl) velocity profiles are also presented. The cloud in the tangential velocity profiles represents all the tangential velocities possible from the averaged image at this position 17, and the tangential velocities show a large scatter which is likely due to a shear layer. Figure 26 shows a similar plot for position 22, where averaging was performed with images #2, #3 and #8.

To determine a tangential velocity profile, an appropriate method for choosing cutting axis is needed, and it would take into account the least noisy flow field where the influence of other neighboring vortices or shear layers is minimized. Practically, a perfectly concentric flow field around the vortex core is not feasible and the judgment about the quality of the vortical flow field is also subject to a researcher‗s experience. A common approach for determining the cutting axis (horizontal, vertical, in between, or a combination of these choices) is to choose the axes manually in the region where a cleaner vorticity field is observed. For example, the optimum cutting axis is selected as the azimuths of 90° and 180° for the positions 17 and 22 as in Figs. 25 and 26, respectively.

The corresponding tabulated data of vortex core radii and tangential velocities are given in Table 8. When the four horizontal and vertical axes (0°, 90°, 180° and 270°) are selected, the mean vortex core radii are 5.3% chord for the position 17 and 10.7% chord for the position 22. The use of the optimum cutting axis at 90° and 180° enables to substantially reduce the vortex core radius compared with the use of the four axes — for a young vortex (position 17) by 40% to 3.2% chord, but for an older vortex

(position 22) it unexpectedly increases the core radius by 7%. The peak tangential velocities with the optimum cutting axes increase by less than 8% for both positions 17 and 22.

Figure 27 is an example of the curve-fit results using a Vatistas model for positions 17 and 22, and the selected cutting axes are 90° and 180° for both positions. For position 17, the core radius was 3.2% chord (= 0.20 %R) with the peak swirl velocity 2.9% of the rotor tip speed. The Vatistas exponent of $n=0.60$ was best-fit to the tangential velocity. For position 22, the core radius was 11.4% chord (= 0.69% R) with the peak swirl velocity 2.58% of the tip speed. The Vatistas exponent was slightly increased to $n=0.70$. Note that the Vatistas exponent may depend on the choice of the cutting axes. This exponent n can be considered as a shape factor for the tangential velocity profile. Since the number of data points within the peak velocity is relatively scarce, Vatistas exponent n may not be highly accurate.

CONCLUSIONS

Despite the past experiences of HART II partners who have dealt with PIV data analyses for years, the complexity of the PIV analysis procedures became readily apparent in the large HART II database. Comparisons of the partners' results typically led to unresolved questions and ambiguity. As a result, the partners focused on a much smaller sample of the database. Although the use of a subset of the PIV database may not be sufficient to establish comprehensive guidelines for establishing a PIV data processing methodology, the effort in this report certainly offers some insights on the PIV data analysis techniques, and helps establish a strong foundation for an analysis methodology. The following are of the main findings from this study:

1) Vortex center identification method – Four methods were used for comparison. The methods were: centroid (AFDD, DLR), Q criterion (ONERA, AFDD, DLR), λ_2 (DLR, AFDD) and convolution of λ_2 (DLR). Although the contours of all the second order velocity gradient tensors (Q criterion, λ_2 and convolution of λ_2) displayed a strong hot spot surrounded with a cleaner flow field compared to the first-order tensor (vorticity), the accuracy of the computed vortex center location was not affected by the order of the tensor. The difference of the vortex center locations among the partners was 1.5 - 1.7% of the chord for position 17, and 2.0 - 3.3% for position 22.

2) Number of individual PIV images – Although the vortex contour was almost unchanged with a variation of the number of images, the peak vorticity value (hot spot) was moderately sensitive. The peak vorticity for position 17 increased by 16% with 38 images (Z=0.5) compared to the value with 89 images (Z=1.5).

3) Sub-grid in vortex center identification – The sub-grid with the top 50% of the peak vorticity showed the vortex center shift by 15% of the chord from the reference value computed with the top 10%. The sub-grid size was important in determining a vortex center, and the top 10% of the maximum vorticity for a sub-grid definition was recommended.

4) Conditional averaging with a subset of the PIV database – Since a subset of the PIV images significantly reduced the problem size, it was possible that each PIV analysis technique was closely examined and accordingly the differences between HART II partners' results were better understood.

5) Rotation angles - The difference of the rotation angles between the averaged images computed using the centroid and convolution of λ_2 was less than 3° for position 22, but the differences between individual images were interestingly larger (6° to 12°).

6) Swirl velocity – The optimum cutting axis for extracting swirl (tangential) velocities was 90° and 180° azimuths for the cases analyzed, which reduced substantially the vortex core radius for a young vortex (position 17) by 40% to 3.2% chord when compared to using four cutting axes (0°, 90°, 180° and 270°). A Vatistas model gave good estimates for swirl velocity profiles.

REFERENCES

1. Raffel, M., Seelhorst, U., and Willert, C., "Vortical Flow Structure at a Helicopter Model Rotor Measured by LDV and PIV," *The Aeronautical Journal of the Royal Aeronautical Society*, Vol. 102, No. 1012, 1998, pp. 221-227.

2. McAlister, K. W., Tung, C., and Heineck, J. T., "Forced Diffusion of Trailing Vorticity from a Hovering Rotor," American Helicopter Society 57th Annual Forum Proceedings, Washington, D. C., May 9-11, 2001.

3. Heineck, J. T., Yamauchi, G. K., Wadcock, A. J., Lourenco, L., and Abrego, A., "Application of Three-Component PIV to a Hovering Rotor Wake," American Helicopter Society 56th Annual Forum Proceedings, Virginia Beach, VA, May 2-4, 2000.

4. Richard, H., and Raffel, M., "Rotor Wake Measurements: Full-Scale and Model Tests", American Helicopter Society 58th Annual Forum Proceedings, Montreal, Canada, May 25-27, 2002.

5. Ramasamy, M., and Leishman, J. G., "A Multi-Region Vortex Model for Transitional Rotor Blade Tip Vortices," *Journal of the American Helicopter Society*, Vol. 51, No. 1, 2006, pp. 92-103.

6. Yamauchi, G. K., Burley, C. L., Mercker, E., Pengel, K., and JanakiRam, R., "Flow Measurements of an Isolated Model Tilt Rotor," American Helicopter Society 55th Annual Forum Proceedings, Montreal, Canada, May 25-27, 1999.

7. Raffel, M., Richard, H., Schneider, G., Klinge, F., Ehrenfried, K., Pengel, K., and Feenstra, G., "Recording and Evaluation Methods of PIV Investigations on a Helicopter Rotor Model", 11th International Symposium on Applications of Laser Techniques to Fluid Mechanics, Lisbon, July 8-11, 2002.

8. Yu, Y. H., Tung, C., van der Wall, B. G., Pausder, J., Burley, C. L., Brooks, T. F., Beaumier, P., Delrieux, Y., Mercker, E., and Pengel, K., "The HART II Test: Rotor Wake and Aeroacoustics with Higher-Harmonic Control Inputs," American Helicopter Society 58th Annual Forum Proceedings, Montreal, Canada, May 25-27, 2002.

9. van der Wall, B. G., Burley, C. L., Yu, Y. H., Pengel, K., and Beaumier, P., "The HART II Test - Measurement of Helicopter Rotor Wakes," *Aerospace Science and Technology*, Vol. 8, No. 4, 2004, pp. 273-284.

10. Lim, J. W., Tung, C., Yu, Y. H., Burley, C. L., Brooks, T. F., Boyd, D., van der Wall, B. G., Schneider, O., Richard, H., Raffel, M., Beaumier, P., Delrieux, Y., Pengel, K., and Mercker, E., "HART II: Prediction of Blade-Vortex Interaction Loading," 29th European Rotorcraft Forum Proceedings, Friedrichshafen, Germany, September 16-18, 2003.

11. van der Wall, B. G., and Richard, H., "Analysis Methodology for 3C PIV Data of Rotary Wing Vortices," *Experiments in Fluids*, Vol. 40, No. 5, 2006, pp. 798-812.

12. Jeong, J., and Hussain, F., "On the Identification of a Vortex," *Journal of Fluid Mechanics*, Vol. 285, 1995, pp. 69-94.

13. van der Wall, B. G., and Burley, C. L., "2nd HHC Aeroacoustics Rotor test (HART II) - Part II: Representative Results," Institute Report IB 111-2005/03, German Aerospace Center (DLR), Braunschweig, Germany, February 2005.

14. Bailly, J., Delrieux, Y., and Beaumier, P., "HART-II: Experimental Analysis and Validation of ONERA Methodology for the Prediction of Blade-Vortex Interaction," 30th European Rotorcraft Forum Proceedings, Marseilles, France, September 14-16, 2004.

15. Tung, C., and Lim, J. W., "Analysis of Rotor Vortex Wake Structure Using 3-C PIV Measurements," *Vortex Dominated Flows*, Chapter 13, edited by Blackmore, Krause, and Tung, World Scientific, Hackensack, NJ, 2005.

16. Burley, C. L., Brooks, T. F., van der Wall, B. G., Richard, H., Raffel, M., Beaumier, P., Delrieux, Y., Lim, J. W., Yu, Y. H., and Tung, C., "Rotor Wake Vortex Definition Using 3C-PIV Measurements – Corrected for Vortex Orientation," AIAA 2003-3175, 9th AIAA/CEAS Aeroacoustics Conference Proceedings, Hilton Head, SC, May 12-14 2003.

17. Hoffmann, F., and van der Wall, B. G., "The Vortex Trajectory Method Applied to HART II PIV Data," Institute Report IB 111-2005/34, German Aerospace Center (DLR), Braunschweig, Germany, August 2005.

18. Raffel, M., Willert, C., Werely, and S., Kompenhans, J., *Particle Image Velocimetry – A Practical Guide*, 2nd edition, Springer Berlin, Heidelberg, New York, 2007.

19. Leishman, J. G., *Principles of Helicopter Aerodynamics*, Cambridge University Press, Cambridge, United Kingdom, 2000.

20. Lamb, H., *Hydrodynamics*, Cambridge University Press, Cambridge, United Kingdom, 1932.

21. Vatistas, G. H., Kozel, V., and Mih, W. C., "A Simpler Model for Concentrated Vortices," *Experiments in Fluids*, Vol. 11, No. 1, 1991, pp. 73-76.

22. van der Wall, B. G., "Comparison of 3C PIV Data Analysis, BL Case," US/German MoU on Helicopter Aeromechanics 55th meeting, Braunschweig, Germany, October 17-18, 2005.

Table 1. Vortex properties of the PIV image at position 17

a) Conditionally averaged properties

	centroid [a]	Q criterion [o]	λ_2 [a]	conv λ_2 [d]	Δ_{max}
γ_{max}/Ω	33.1	30.8	32.7	31.5	2.3
x_v/R (%)	0.41	0.43	0.40	0.44	0.04
y_v/R (%)	0.52	0.52	0.52	0.54	0.02
σ_x/R (%)	0.60	-- [*]	0.61	0.13	0.48
σ_v/R (%)	0.29	-- [*]	0.30	0.11	0.19

b) Difference in the averaged property, referenced from a centroid

	centroid [a]	Q criterion [o]	λ_2 [a]	conv λ_2 [d]
$\Delta\gamma_{max}/\Omega$ (%)	-- [r]	-6.9	-1.2	-4.8
$\Delta x_v/c$ (%)	-- [r]	0.26	-0.15	0.46
$\Delta y_v/c$ (%)	-- [r]	-0.03	-0.18	0.28

[a] provided by AFDD, [o] provided by Onera, [d] provided by DLR, [r] reference data,
[*] no data provided

Table 2. Vortex properties of the PIV image at position 22

a) Conditionally averaged properties

	centroid [a]	Q criterion [o]	λ_2 [a]	conv λ_2 [d]	Δ_{max}
γ_{max}/Ω	24.8	25.6	24.9	25.2	0.8
x_v/R (%)	-0.08	0.04	-0.08	-0.13	0.17
y_v/R (%)	0.03	-0.17	0.04	0.01	0.21
σ_x/R (%)	0.76	-- [*]	0.76	0.57	0.19
σ_v/R (%)	0.46	-- [*]	0.46	0.41	0.05

b) Difference in the averaged property, referenced from a centroid

	centroid [a]	Q criterion [o]	λ_2 [a]	conv λ_2 [d]
$\Delta\gamma_{max}/\Omega$ (%)	-- [r]	1.6	0.4	1.6
$\Delta x_v/c$ (%)	-- [r]	1.98	0.0	-0.83
$\Delta y_v/c$ (%)	-- [r]	-3.31	0.17	-0.33

[a] provided by AFDD, [o] provided by Onera, [d] provided by DLR, [r] reference data,
[*] no data provided

Table 3. Z score, the number of images and the maximum vorticity for the PIV image at position 17 when the centroid method is employed

Z score	# of images	γ_{max}/Ω	$(\gamma-\gamma_{Z=1.5})/\gamma_{Z=1.5}$
0.5	38	38.3	15.7%
0.7	62	36.5	10.3%
1.5	89	33.1	-- [r]
5.0	99	31.7	-4.2%

[r] reference data

Table 4. Vortex properties derived with the individual PIV images #1 and #3 at position 17

a) Image #1

	centroid [a]	Q criterion [o]	conv λ_2 [d]	Δ_{max}
γ_{max}/Ω	51.9	52.6	52.6	0.7
x_v/R (%)	0.31	0.35	0.29	0.06
y_v/R (%)	0.52	0.52	0.53	0.01

b) Image #3

	centroid [a]	Q criterion [o]	conv λ_2 [d]	Δ_{max}
γ_{max}/Ω	34.1	34.1	34.1	0.0
x_v/R (%)	0.35	0.35	0.43	0.08
y_v/R (%)	0.75	0.75	0.73	0.02

c) Conditional averaging with images #1 and #3

	centroid [a]	Q criterion [o]	conv λ_2 [d]	Δ_{max}
γ_{max}/Ω	43.3	43.4	47.7	4.4
x_v/R (%)	0.33	-- [*]	0.36	0.03
y_v/R (%)	0.64	-- [*]	0.64	0.0

d) Difference in conditionally averaged property with images #1 and #3, referenced from the results of a centroid

	centroid [a]	Q criterion [o]	conv λ_2 [d]
$\Delta\gamma_{max}/\Omega$ (%)	-- [r]	0.2	10.2
$\Delta x_v/c$ (%)	-- [r]	-- [*]	0.50
$\Delta y_v/c$ (%)	-- [r]	-- [*]	0.0

[a] provided by AFDD, [o] provided by Onera, [d] provided by DLR, [r] reference data, [*] no data provided,

Table 5. Vortex properties derived with the individual PIV images #2, #3 and #8 at position 22

a) Conditional averaging

	centroid [a]	conv λ_2 [d]	Δ_{max}
γ_{max}/Ω	24.4	23.3	1.1
x_v/R (%)	-0.29	-0.34	0.05
y_v/R (%)	0.35	0.37	0.02

b) Difference in conditionally averaged property, referenced from a centroid

	centroid [a]	conv λ_2 [d]
$\Delta\gamma_{max}/\Omega$ (%)	-- [r]	4.5
$\Delta x_v/c$ (%)	-- [r]	0.83
$\Delta y_v/c$ (%)	-- [r]	0.33

[a] provided by AFDD, [d] provided by DLR, [r] reference data

Table 6. Rotation angles computed with the individual PIV images #2, #3 and #8 at position 22

a) Image-to-image (i2i) difference

	centroid [a]	conv λ_2 [d]
$\Delta\theta_{x,i2i}$	7.7^o	12.3^o
$\Delta\theta_{y,i2i}$	6.2^o	5.2^o

b) Conditional average (ca)

	centroid [a]	conv λ_2 [d]	Δ_{max}
$\theta_{x,ca}$	6.3^o	8.3^o	2.0^o
$\theta_{y,ca}$	-34.3^o	-31.4^o	2.9^o

[a] provided by AFDD, [d] provided by DLR

Table 7. Rotation angles computed from the conditionally averaged image with all 100 PIV images at positions 17 and 22

a) Pos 17

	centroid [a]	Q criterion [o]	conv λ_2 [d]
$\theta_{x,ca}$	-0.7°	1.6°	4.3°
$\theta_{y,ca}$	-19.4°	-25.7°	-19.2°

b) Pos 22

	centroid [a]	Q criterion [o]	conv λ_2 [d]
$\theta_{x,ca}$	2.2°	-1.4°	12.4°
$\theta_{y,ca}$	-33.9°	-20.6°	-22.6°

[a] provided by AFDD, [o] provided by Onera, [d] provided by DLR

Table 8. Vortex core radii and tangential velocities at positions 17 and 22, averaged (centroid) with a few selected images

cutting axis	Pos 17		Pos 22	
	r_c/c (%)	$v_{\theta,max}/\Omega R$ (%)	r_c/c (%)	$v_{\theta,max}/\Omega R$ (%)
0°	4.8	2.4	10.4	2.1
90°	2.8	3.0	12.4	2.6
180°	3.6	2.9	10.4	2.6
270°	10.1	2.6	9.8	2.5
mean (0°,90°,180°,270°)	5.3	2.7	10.7	2.4
optimum mean (90°, 180°)	3.2	2.9	11.4	2.6
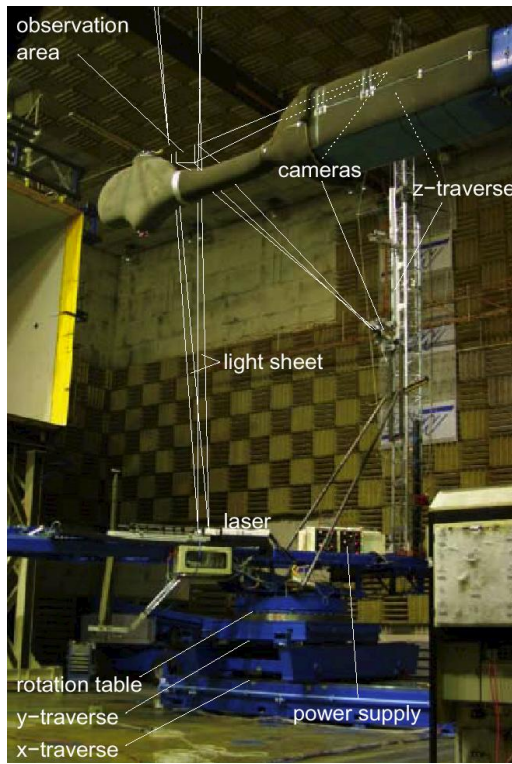
Figure 1. HART rotor and 3-C PIV test set-up
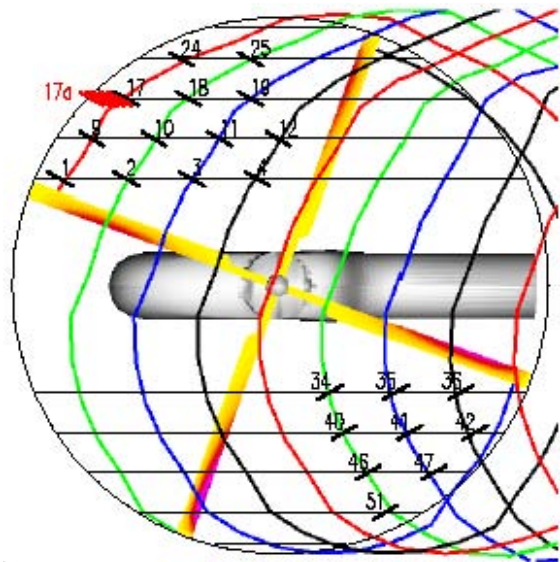
a) Reference blade at 70 degrees
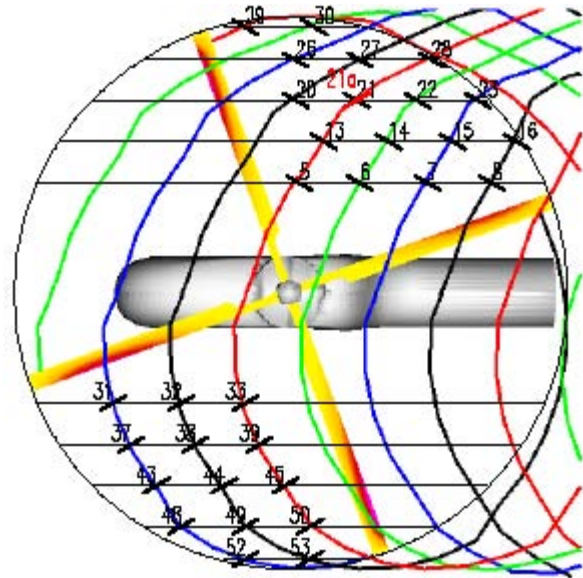
b) Reference blade at 20 degrees

Figure 2. Schematic diagram for PIV measurement planes
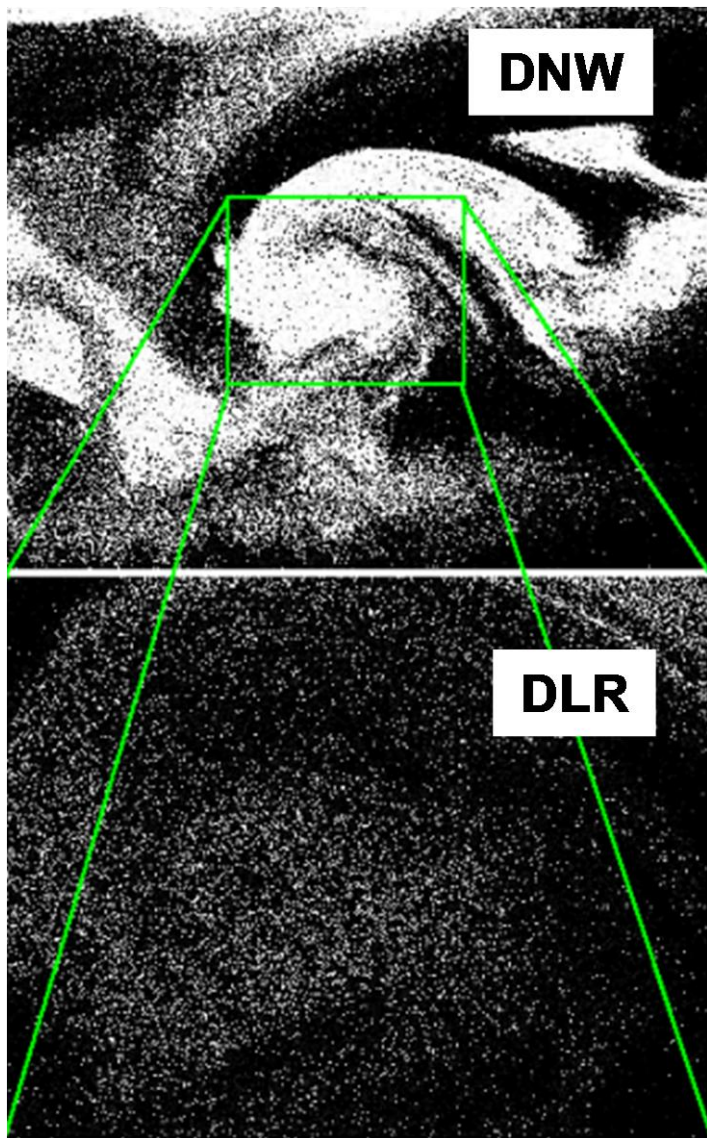
Figure 3. Raw image from two different cameras for the
baseline case, position 21.
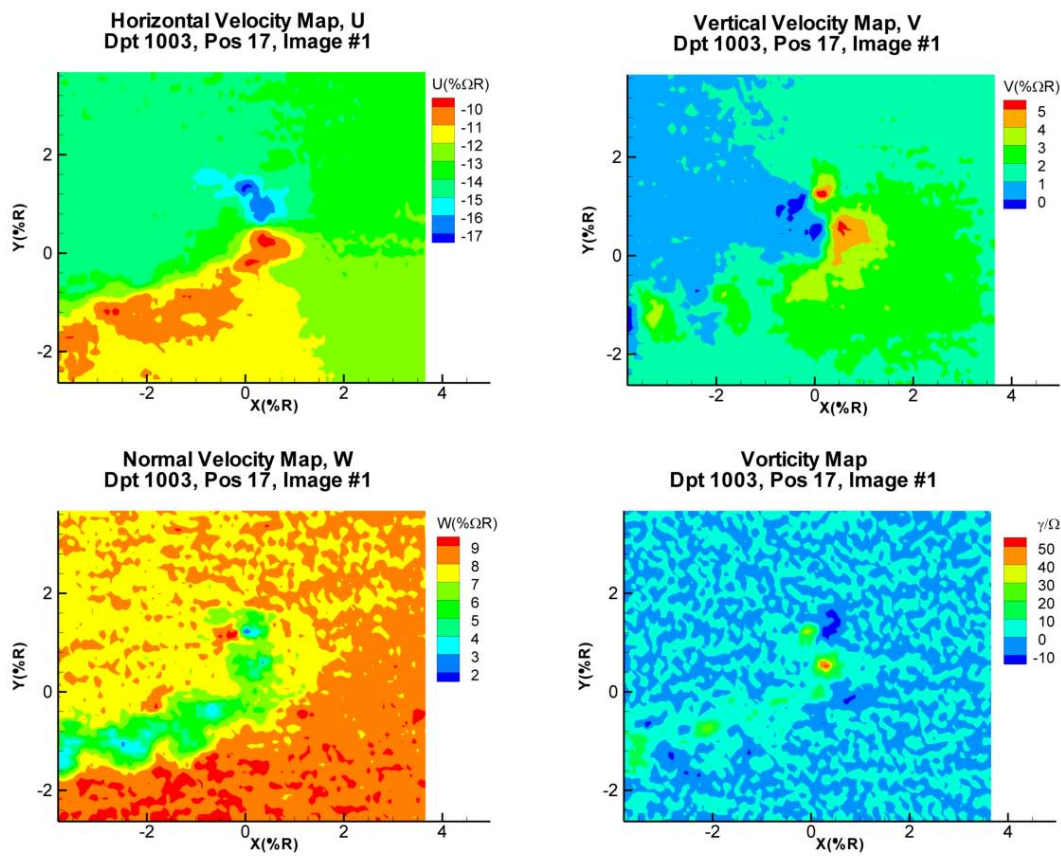
Figure 4. Single PIV image of 3-C velocity and vorticity map (image #1) for position 17 (Dpt 1003) with an age of 25.3°.
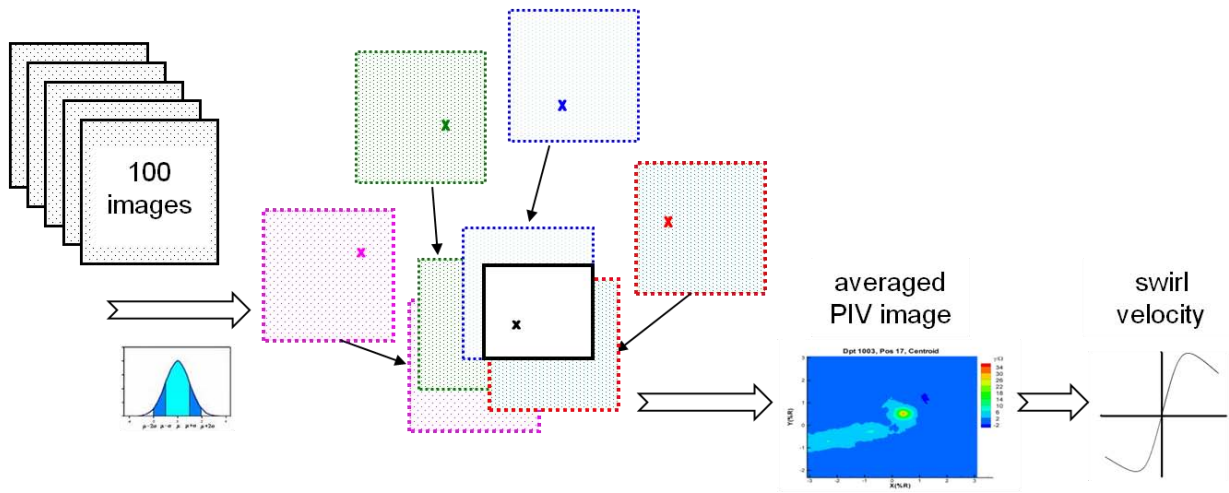
Figure 5. Conditional averaging procedure
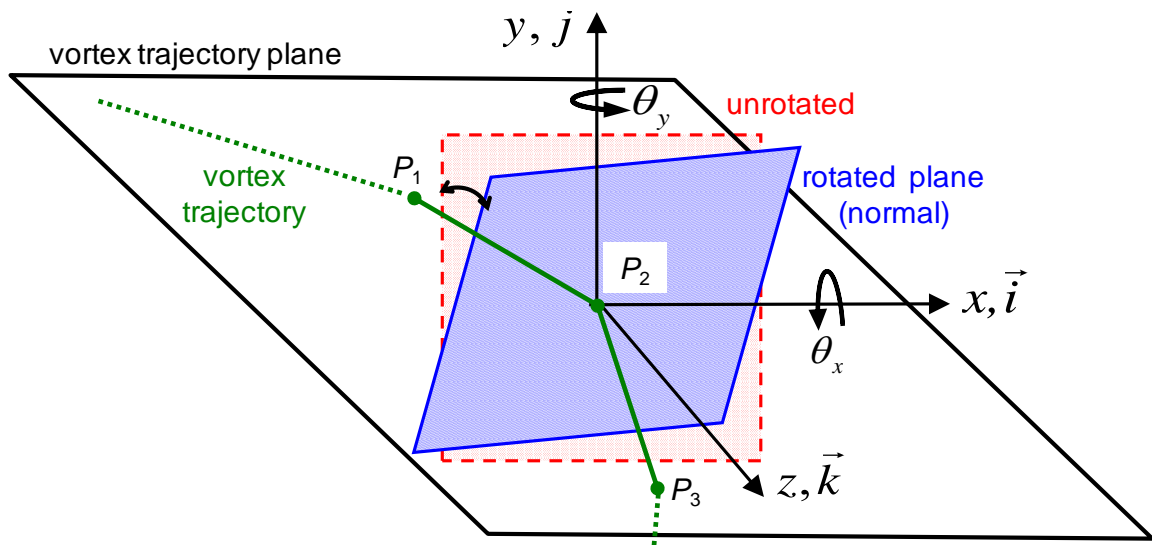
Figure 6. Re-orientation of the PIV measurement plane for the vortex trajectory method.
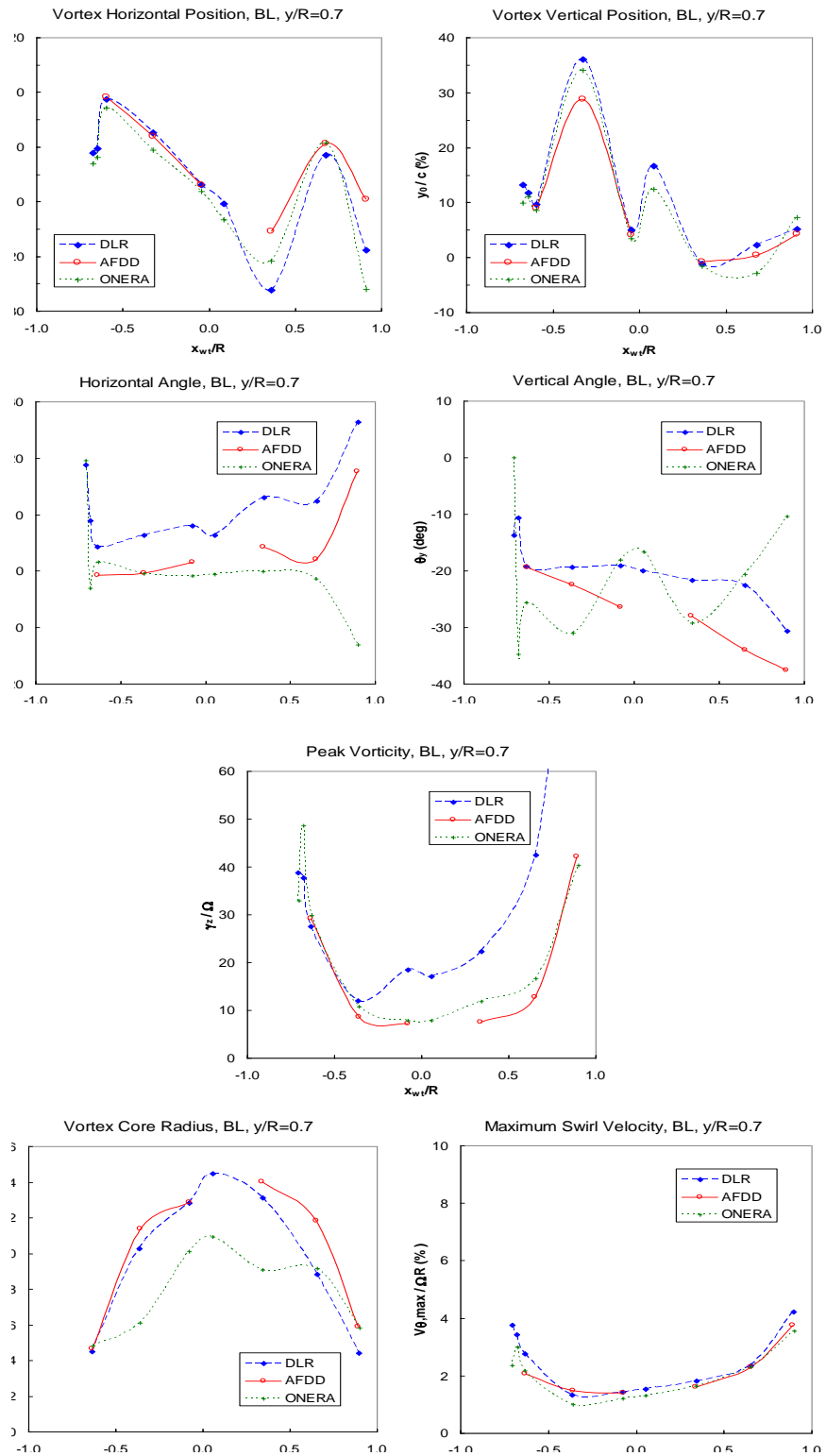
Figure 7. Comparison of vortex properties among HART II partners' results in the longitudinal plane of y/R=0.7 on the advancing side (baseline, positions 17-23)
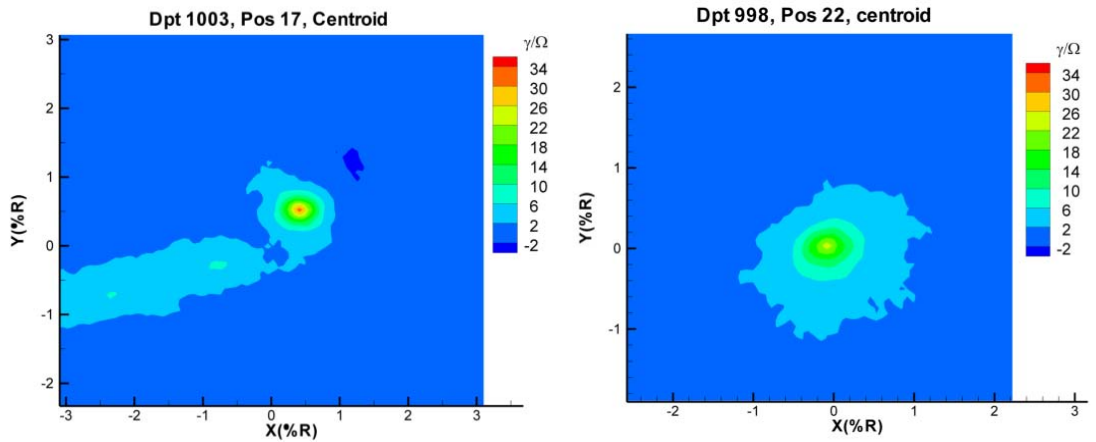
Figure 8. Conditionally averaged vorticity maps (unrotated) for positions 17 (Dpt 1003, wake age of 25.3°) and 22 (Dpt 998, wake age of 425.3°).
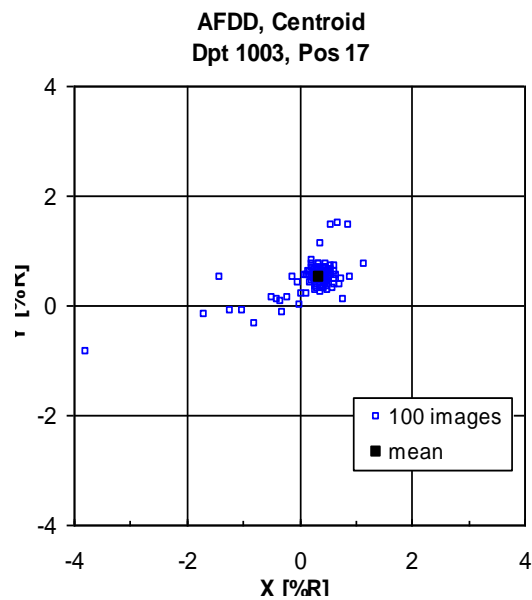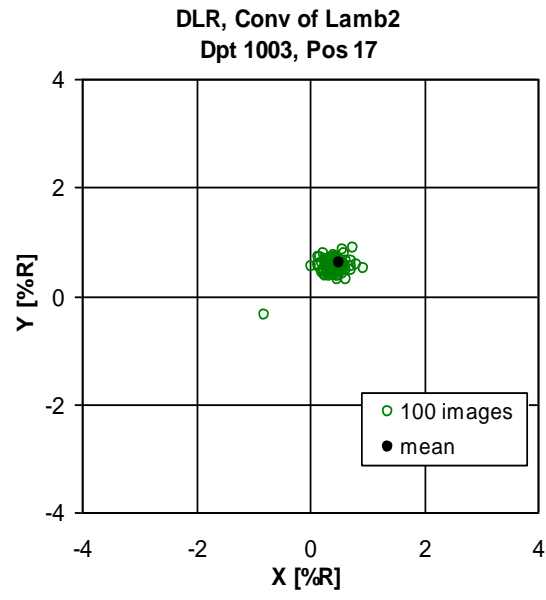
a) centroid   b) convolution of λ_2

Figure 9. Vortex center distribution of all 100 individual images for position 17 (Dpt 1003).
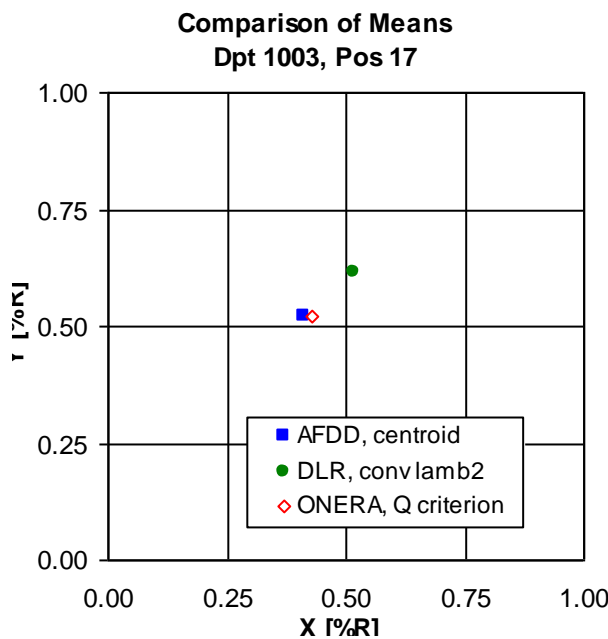
Figure 10. A comparison of the mean vortex center derived using centroid, Q criterion and convolution of λ_2 for position 17 (Dpt 1003).
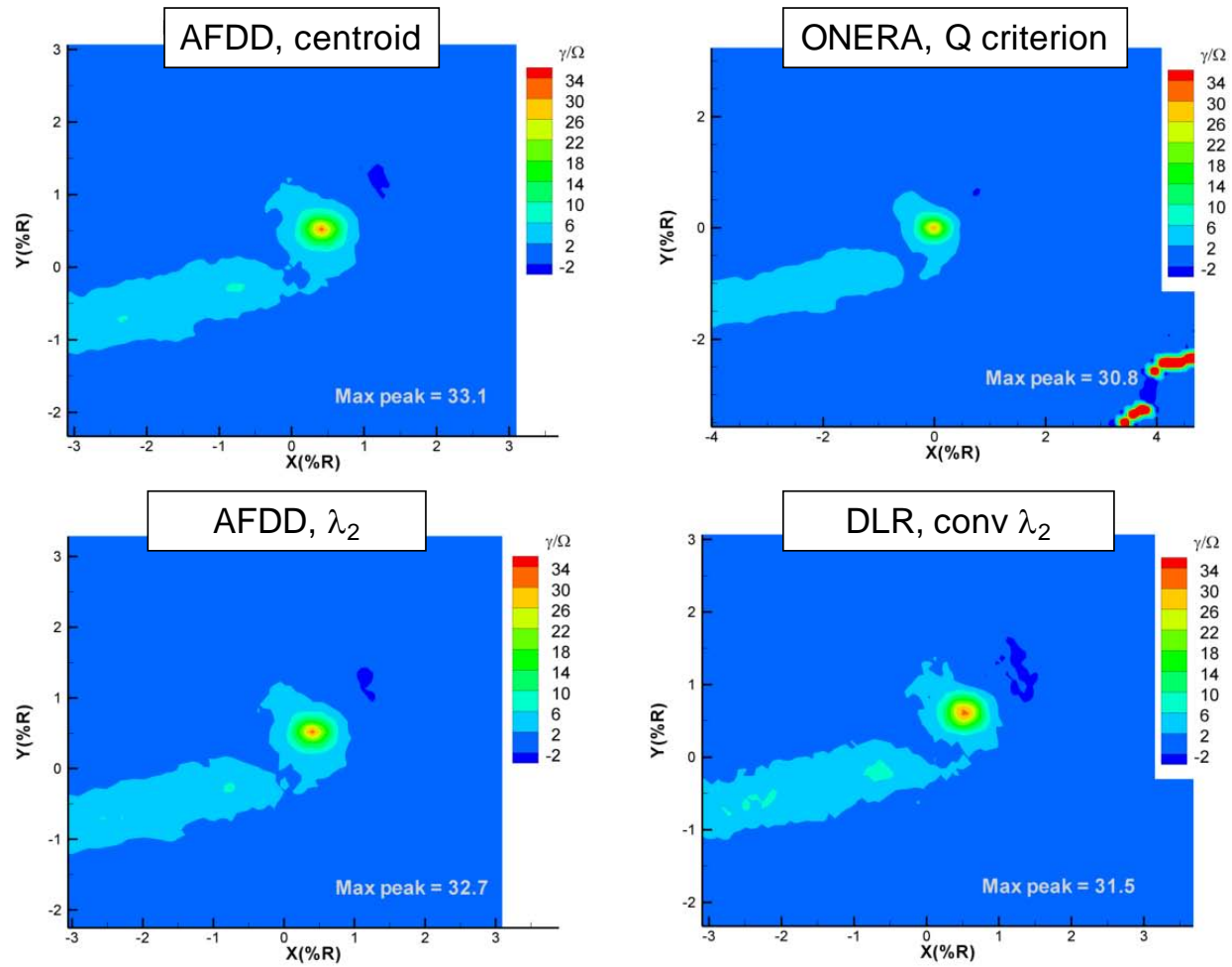
Figure 11. Comparison of conditionally averaged vorticity (γ/Ω) using various center identification methods for position 17 (Dpt 1003).
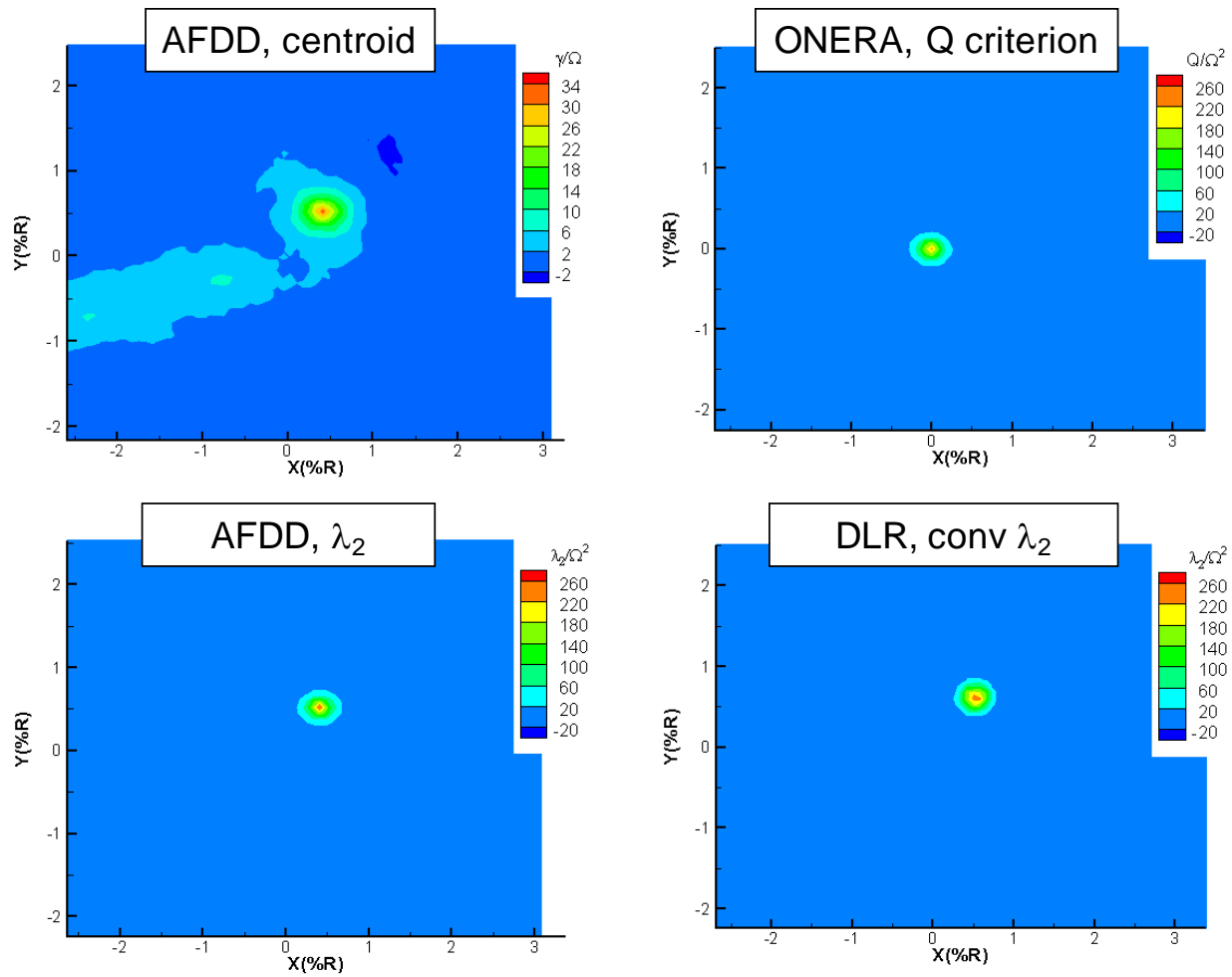
Figure 12. Comparison of conditionally averaged velocity gradient tensors - centroid, Q criterion, λ_2, and convolution of λ_2 - using various center identification methods for position 17 (Dpt 1003).
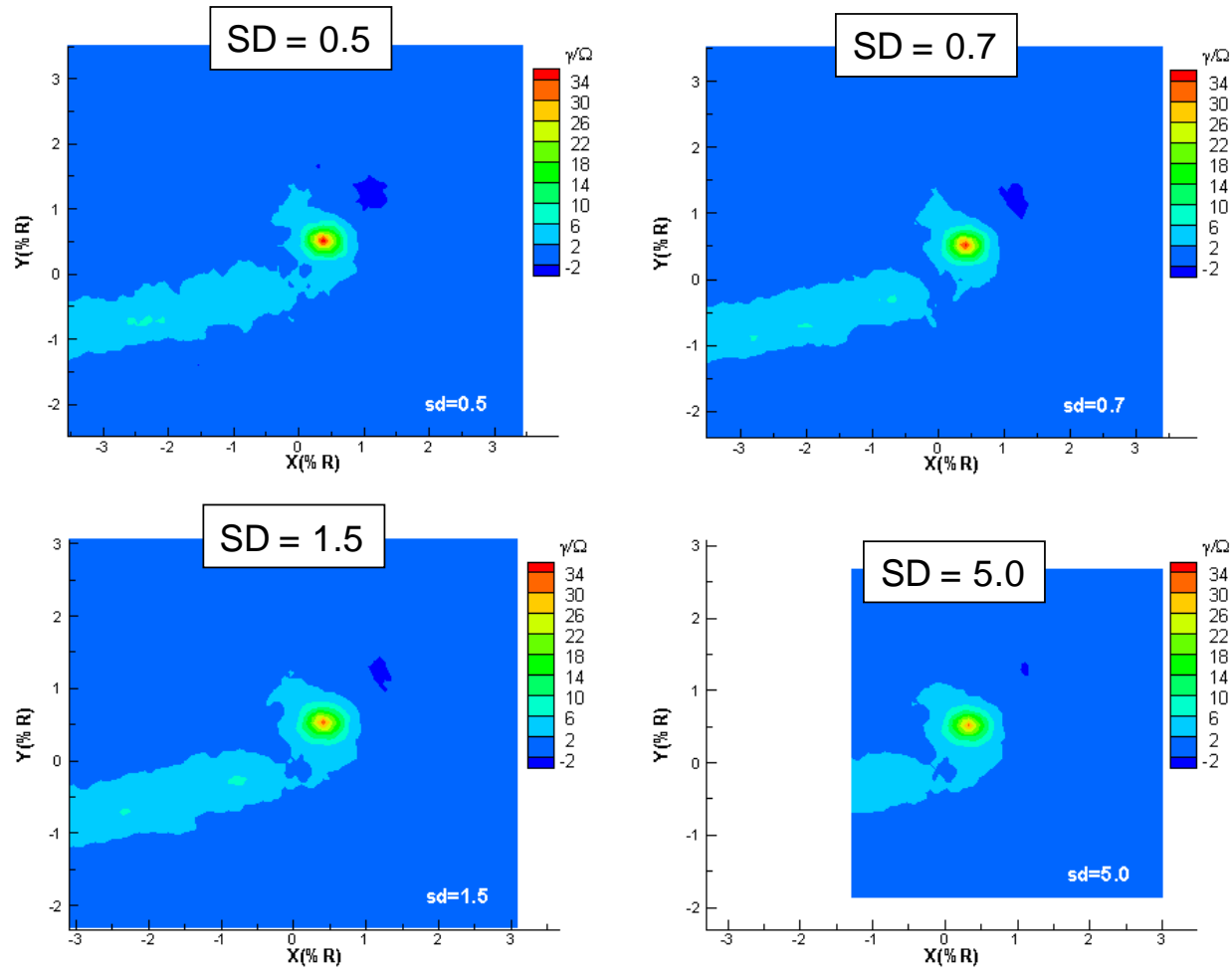
Figure 13. Effect of Z scores or standard deviation of vortex center on the conditionally averaged vorticity for position 17 (Dpt 1003): standard deviations of 0.5, 0.7, 1.5, and 5.0.
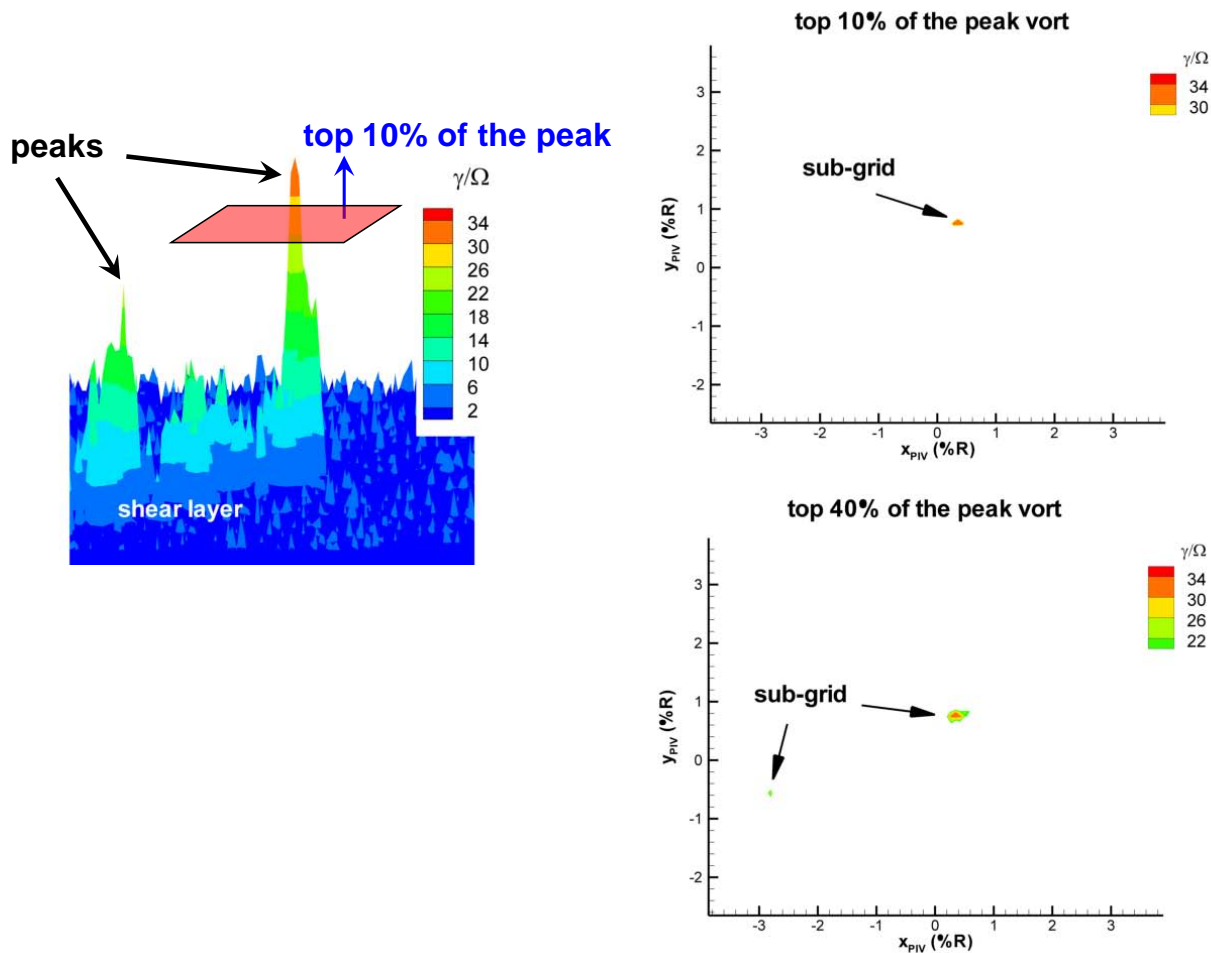
Figure 14. A perspective view of the vorticity map and the locations of its sub-grids in the PIV image #3 for position 17 (Dpt 1003) in the baseline case.
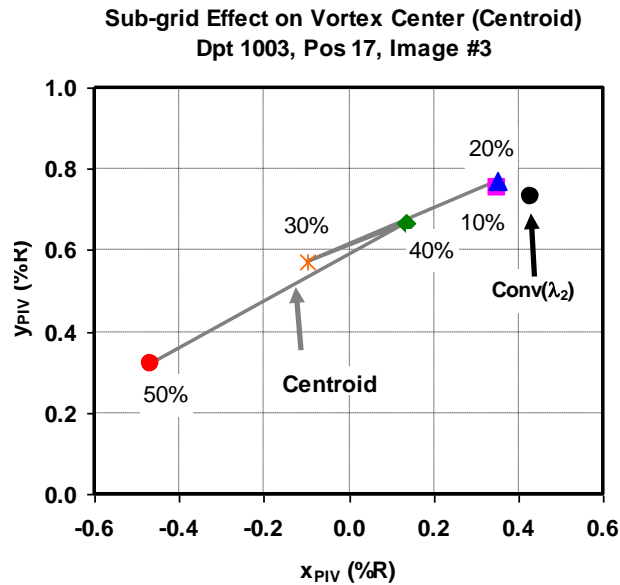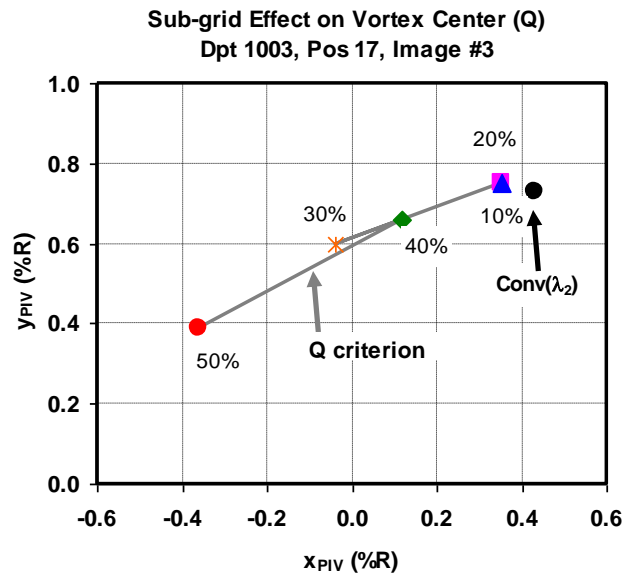
a) Centroid   b) Q criterion

Figure 15. Vortex centers with a variation of the sub-grid size for the PIV image #3 for position
17 (Dpt 1003).
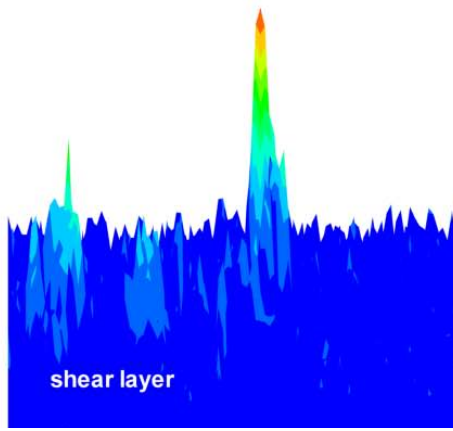
a) Perspective view of λ_2
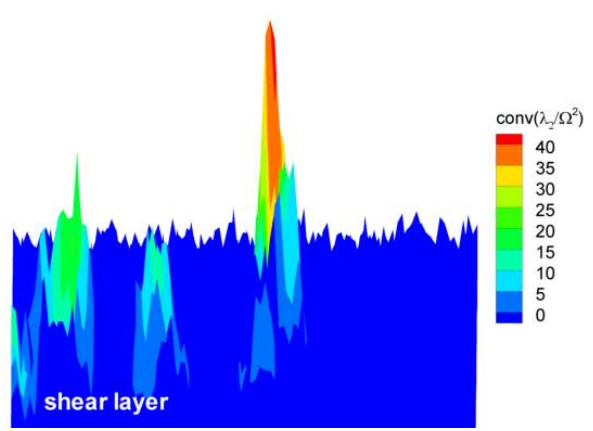
c) Perspective view of convolution of λ_2
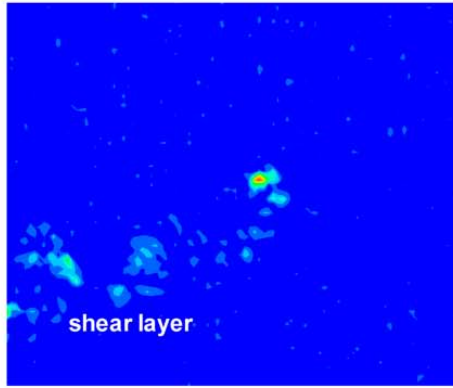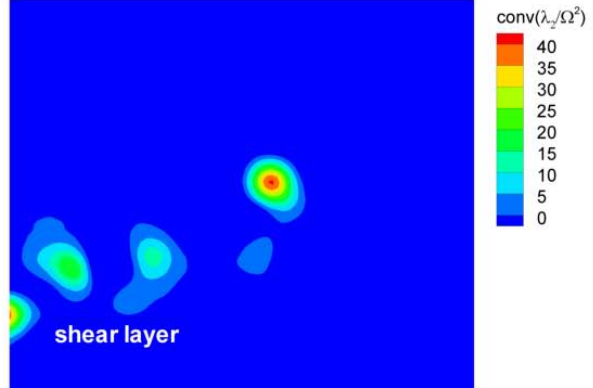
b) Top view of λ_2

d) Top view of convolution of λ_2

Figure 16. Perspective and top views of λ_2 and convolution of λ_2 in the PIV image #3 for position 17 (Dpt 1003) in the baseline case.
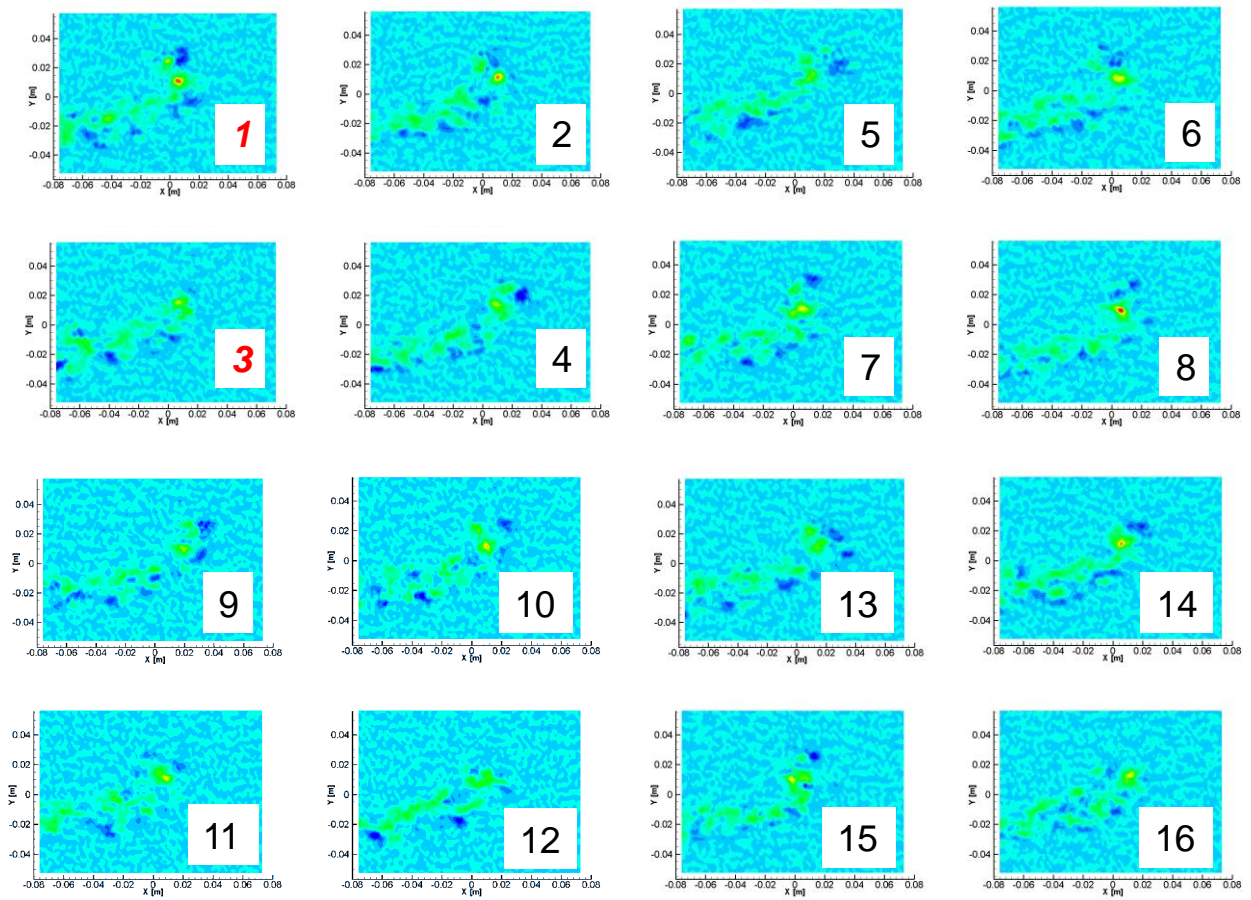
Figure 17. The first 16 individual PIV images at position 17 (Dpt 1003) in the baseline case.

BL, Pos 17, image #1

BL, Pos 17, image #1
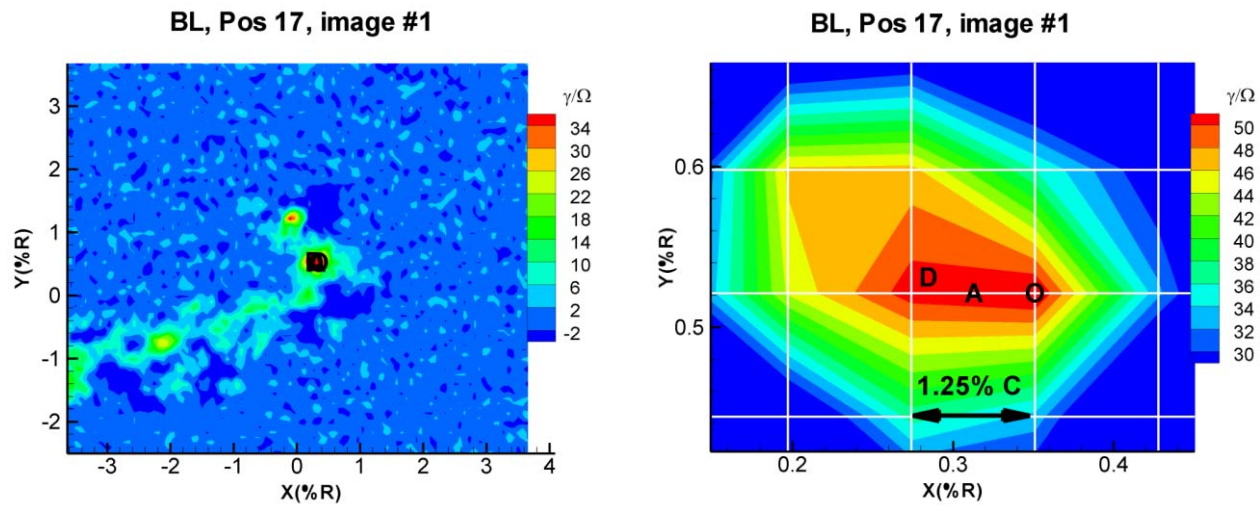
Figure 18. Individual Image #1: position 17 (Dpt 1003).

BL, Pos 17, image #3

BL, Pos 17, image #3
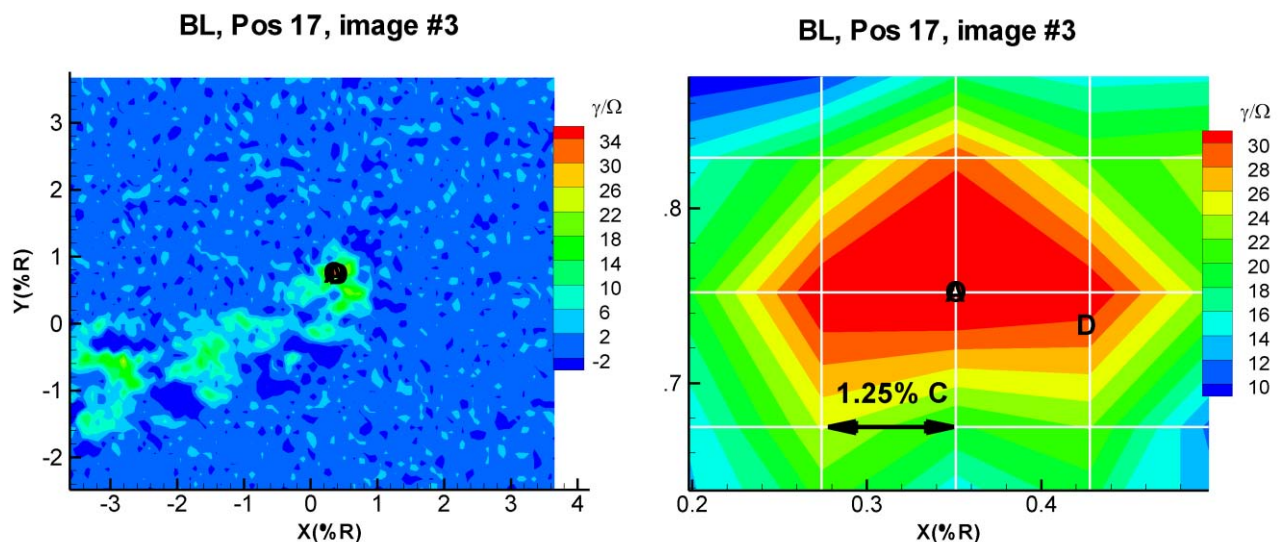
Figure 19. Individual Image #3: position 17 (Dpt 1003).
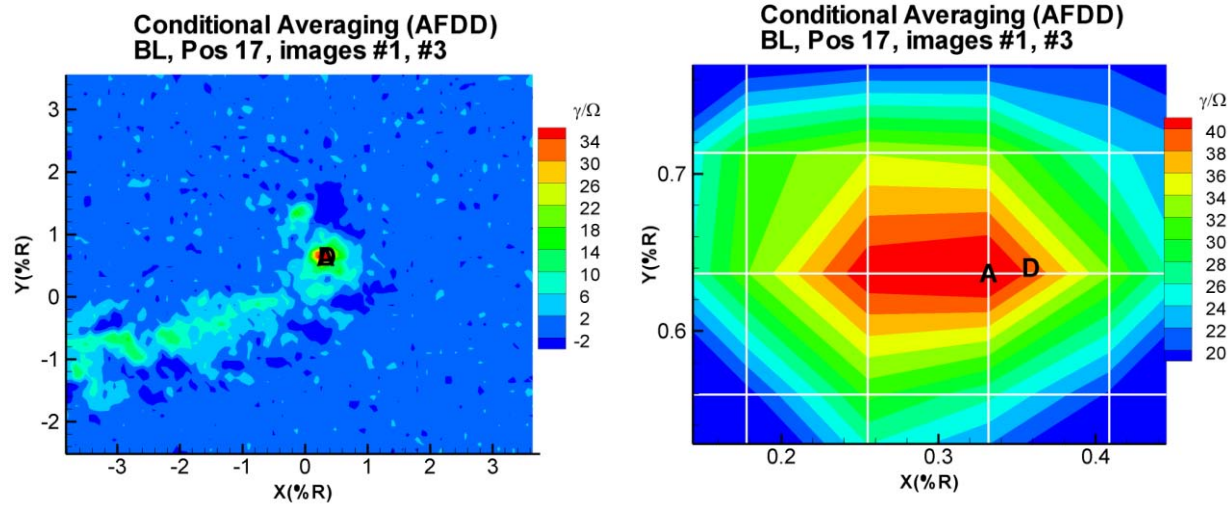
Figure 20.Conditional averaging with images #1 and #3: position 17 (Dpt 1003).
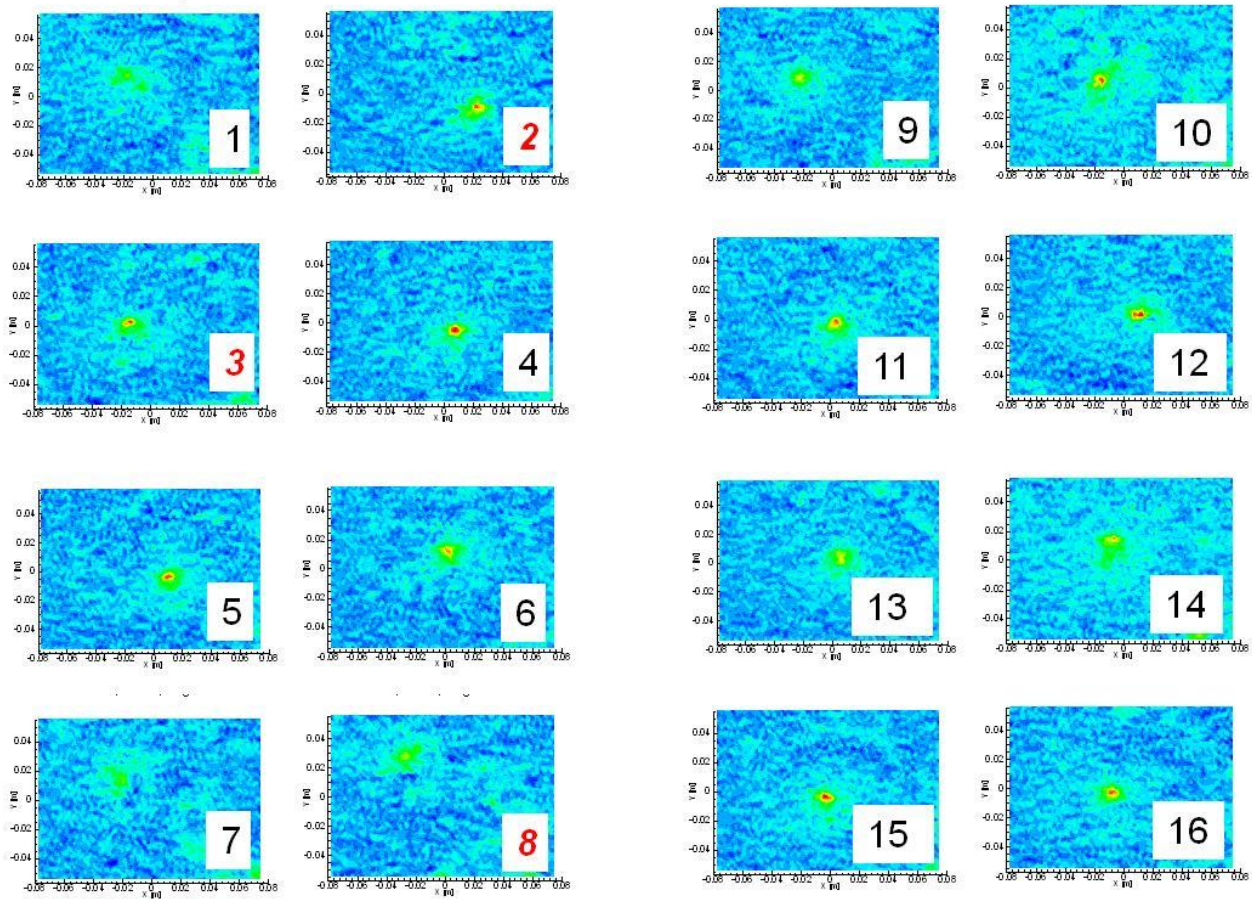
Figure 21. The first 16 individual PIV images: position 22 (Dpt 998).
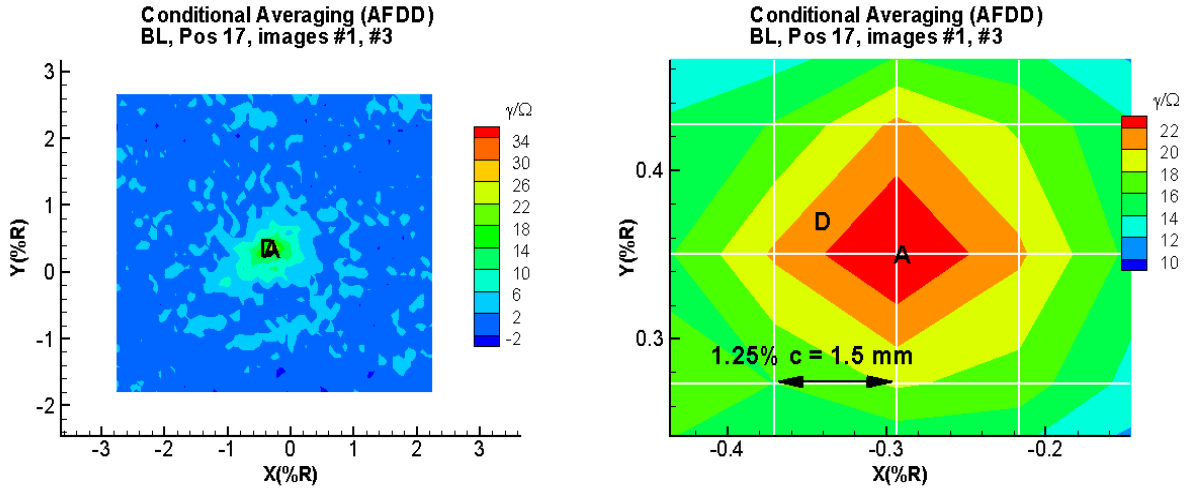
Figure 22. Conditional averaging with images #2, #3 and #8: position 22 (Dpt 998).
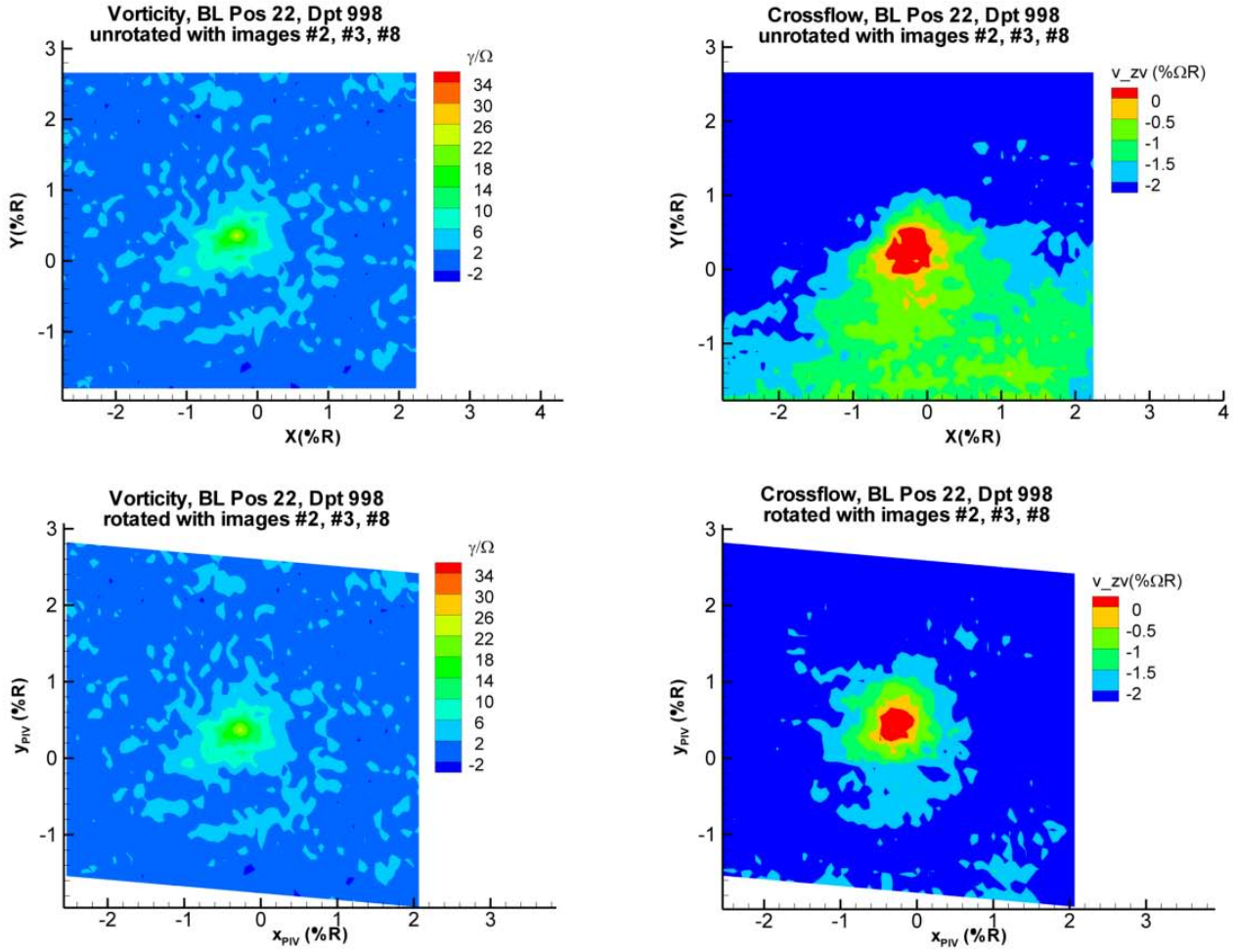

Figure 23. The vorticity (γ/Ω) and cross flow ($v_z/\Omega R$) averaged with images #2, #3 and #8 for position 22 (Dpt 998) before and after the rotation.
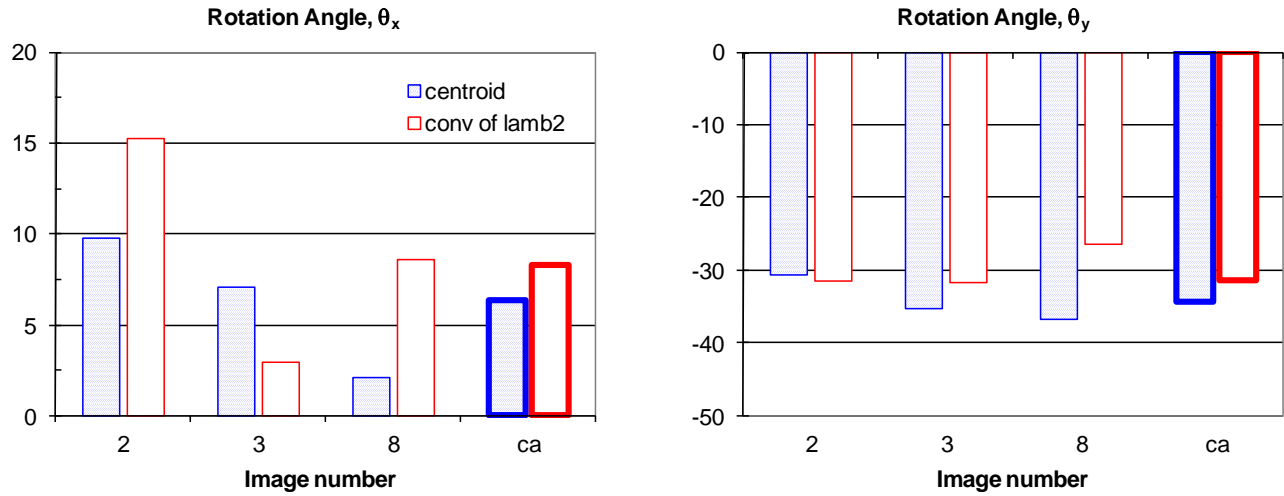
Figure 24. A comparison of the centroid and convolution of λ_2 rotation results for each individual image, #2, #3 and #8 and its averaged image for position 22 (Dpt 998). The label, "ca" is the conditionally averaged image.


a) Vorticity
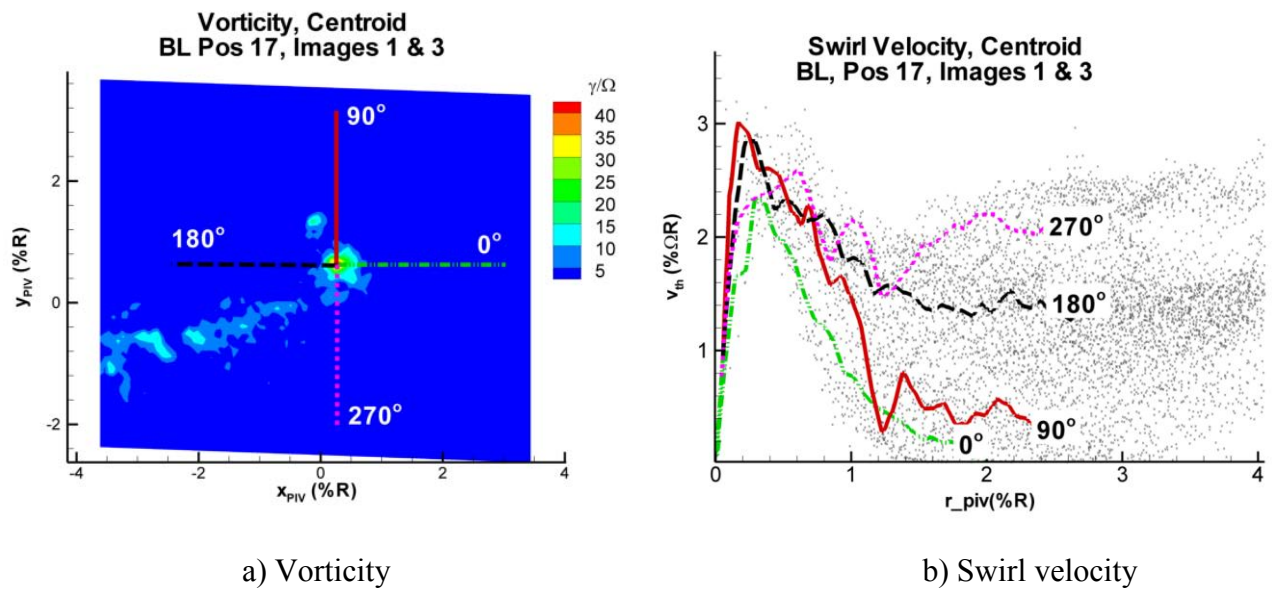
b) Swirl velocity

Figure 25. Cutting axes in the vorticity map and the associated tangential velocities at 0°, 90°, 180° and 270° for position 17 (Dpt 1003).
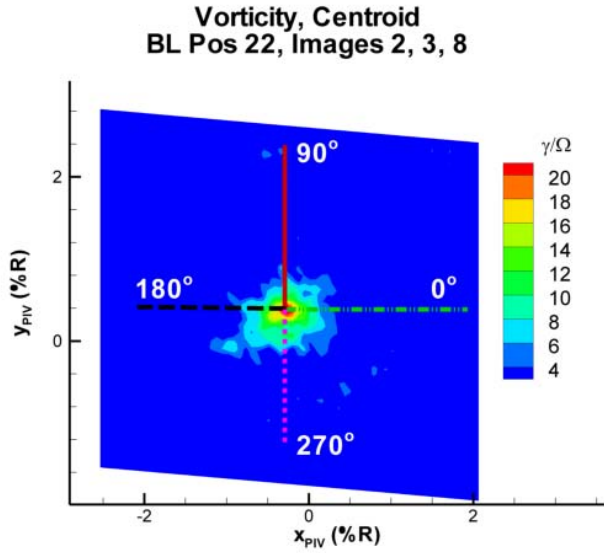
a) Vorticity
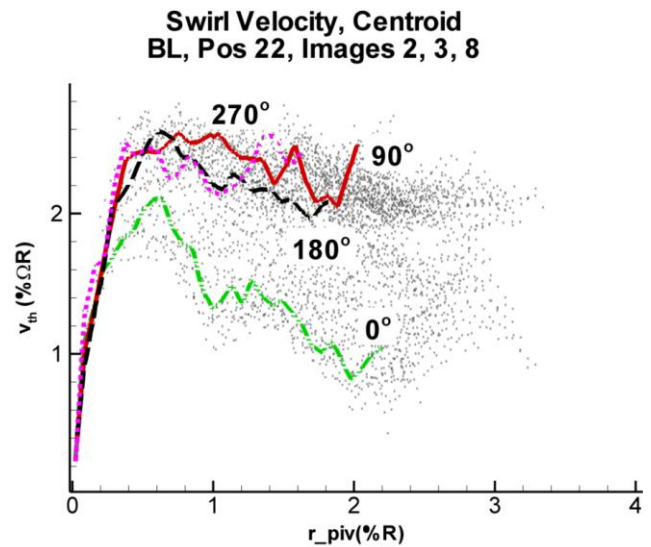
b) Swirl velocity

Figure 26. Cutting axes in the vorticity map and the associated tangential velocities at 0°, 90°, 180° and 270° for position 22 (Dpt 998).
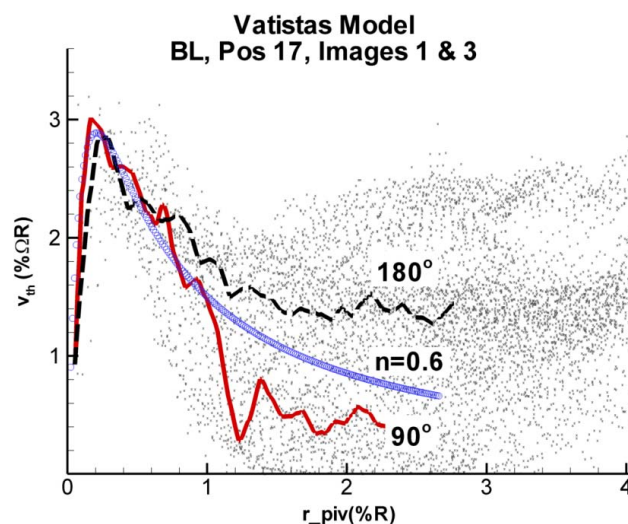
a) Position 17
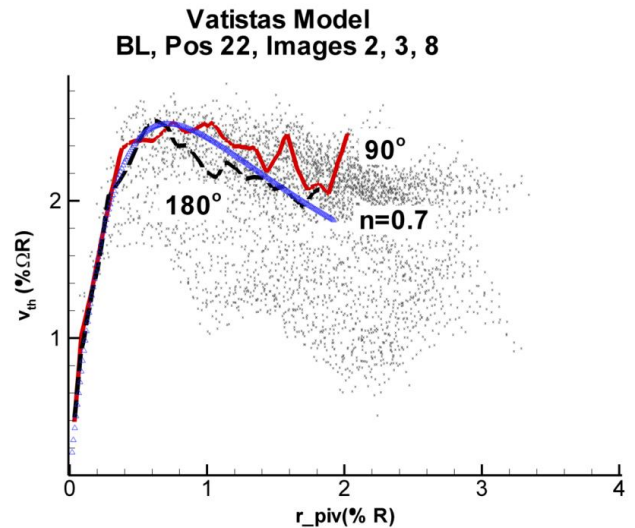
b) Position 22

Figure 27. Swirl velocities using a Vatistas model of the prototyped images for positions 17 and 22.

INITIAL DISTRIBUTION LIST

		Copies
Weapon Systems Technology Information Analysis Center Alion Science and Technology 201 Mill Street Rome, NY 13440	Ms. Perry E. Onderdonk ponderdonk@alionscience.com	Electronic
Defense Technical Information Center 8725 John J. Kingman Rd., Suite 0944 Fort Belvoir, VA 22060-6218	Mr. Jack L. Rike jrike@dtic.mil	Electronic
AMSAM-LI,	Ms. Anne C. Lanteigne anne.lanteigne@us.army.mil	Electronic
RDMR		Electronic
RDMR-CSI		Electronic
RDMR-AF	Mr. Barry R. Lakinsmith barry.r.lakinsmith@us.army.mil	Electronic
	Mr. Thomas Maier maier@merlin.arc.nasa.gov	Electronic
	Mr. Richard F. Spivey Richard.f.spivey@us.army.mil	Electronic
Bell Helicopter Textron	Mr. J. Narramore jnarramore@bellhelicopter.textron.com	Electronic
Boeing Company	Mr. Leo Dadone Leo.dadone@boeing.com	Electronic
	Dr. Ram Janakiram ram.d.janakiram@boeing.com	Electronic
	Dr. Mathew B. Mathew mathew.b.mathew@boeing.com	Electronic

NASA Ames Research Center	Mr. James T. Heineck james.t.heineck@nasa.gov	Electronic
	Dr. Manikandan Ramasamy mramasamy@merlin.arc.nasa.gov	Electronic
	Dr. Alan J. Wadcock alan.j.wadcock@nasa.gov	Electronic
	Dr. Gloria Yamauchi K. gloria.k.yamauchi@nasa.gov	Electronic
NASA Langley Research Center	Ms. Casey L. Burley casey.l.burley@nasa.gov	Electronic
	Ms. Susan A. Gorton susan.a.gorton@nasa.gov	Electronic
	Mr. Luther N. Jenkins Luther.n.Jenkins@nasa.gov	Electronic
	Dr. Chung-Sheng Yao c.s.yao@nasa.gov	Electronic
Sikorsky Aircraft	Dr. Ashish Bagai abagai@sikorsky.com	Electronic
	Mr. Alan Egolf tegolf@sikorsky.com	Electronic
Additional Distribution	Mr. Philippe Beaumier philippe.beaumier@onera.fr	Electronic
	Ms. Blanche Demaret blanche.demaret@onera.fr	Electronic
	Mr. Yves Delrieux yves.delrieux@onera.fr	Electronic
	Ms. Frauke Hoffmann rfrauke.hoffman@dlr.de	Electronic
	Mr. Klausdieter Phalke klausdieter.pahlke@dlr.de	Electronic
	Dr. Markus Raffel markus.raffel@dlr.de	Electronic
	Dr. Berend van der Wall berend.vanderwall@dlr.de	Electronic
	Ms. Joelle Zibi joelle.zibi@onera.fr	Electronic